Spectrum imaging of complex nanostructures using DualEELS: II. Absolute quantification using standards

Alan J. Craven, Bianca Sala, Joanna Bobynko and Ian MacLaren

School of Physics and Astronomy, University of Glasgow, Glasgow G12 8QQ, UK

ABSTRACT

Nanometre-sized $Ti_xV_{(1-x)}C_yN_z$ precipitates in an Fe20%Mn steel matrix with a thickness range from 14 to 40 nm are analysed using DualEELS. Their thicknesses, volumes and compositions are quantified using experimental binary standards and the process used to give robust results is described. Precisions of a few per cent are achieved with accuracies that are estimated to be of a similar magnitude. Sensitivities are shown to be at 0.5-1 unit cells range in the thinnest matrix region, based on the assumption that a sub-lattice is fully populated by the element. It rises to the 1-2 unit cell range for the metals and 2-3 unit cells for the non-metal in the thickest matrix region. The sensitivities for Ti and N are greater than those for V and C respectively because the O K-edge from surface oxide needs to be separated from the V $L_{2,3}$-edge, and the C K-edges from C in the matrix and amorphous C on the surface have to be separated from the C in the precipitate itself. Separation of the contributions from the bulk and the surface is demonstrated, showing that there is significant and detectable C in the matrix but no O, while there is significant O but little C in the surface oxide. Whilst applied to precipitates in steel in this work, the approach can be adapted to many multi-phase systems.

1. Introduction

The characterisation of the chemistry of precipitates buried in a matrix is an important but difficult problem, for example in understanding the effect of alloying and thermomechanical processing on precipitation in steels. The challenges are similar to those found in other materials problems e.g. catalyst nano-particles on a support. Traditionally, the main method for the characterisation of precipitates has been the use of an extraction replica. Here the sample is polished, etched to expose precipitates, coated in a thin film (typically amorphous carbon) and re-etched to free the precipitates. The thin film adheres to the precipitates and can be floated off to be mounted on a TEM grid. Whilst this is an excellent method for extracting large numbers of precipitates from large areas and thereby getting useful statistics about size distributions, there are also concerns. The extraction efficiency can vary with precipitate size [1-4]. The precipitates can be partially dissolved or have their

composition altered in the processing [5]. The relationships between the precipitates and the matrix are also lost. Extraction using a carbon film also causes problems when analysing carbides but there are ways to mitigate this but they may modify the precipitates [6]. Other materials have also been used successfully for the film e.g. Al, amorphous Al_2O_3 and a-Si [5, 7-10].

In a previous paper [11] it is shown that the electron energy loss spectroscopy (EELS) signal from a precipitate contained in a thin sample of a steel can be separated from that of the surrounding matrix using spectrum imaging and DualEELS. In spectrum imaging, an electron probe is scanned over the sample and one or more spectra are collected at each pixel along with suitable image signals [12]. DualEELS uses a fast electrostatic shutter and deflector to record both the low-loss and core loss regions of the EELS spectrum at each pixel [13, 14].

By splicing the low-loss and high-loss regions of the spectra at each pixel in a spectrum image (SI) and then using Fourier-logarithmic deconvolution, a set of single scattering distributions is obtained. In some areas of the SI, only matrix is present and so an average spectrum from the matrix can be obtained. If the matrix contains one or more elements not present in the precipitate, the precipitate signal can be "extracted".

The challenge for this technique or any other nanoanalysis technique is to quantify the data with high sensitivity and accuracy. The traditional EELS quantification route is well described by Egerton [15]. This is to fit a power law background in a window before the edge, extrapolate it and subtract it. The extracted signal is then integrated over a window, typically with a width in the range of 50 – 100 eV. This signal is divided by the integral over the same window of a calculated cross-section based on either a hydrogenic or Hartree-Slater (HS) model. If the zero-loss intensity is available, as is the case with the data in this paper, the result can be normalised to give the absolute number of atoms per unit area. If not, only the relative amounts of each element present can be determined. There are several issues with this approach. The shapes of the calculated cross-sections differ very significantly from those of the experimental edges giving rise to errors [16]. Where edges are closely spaced, the fine structure on the lower edge perturbs the background for a higher edge, preventing accurate signal extraction. Even when the edges are widely spaced, the extended energy loss fine structure (EXELFS) from lower lying edges can perturb background shapes for higher energy ones [11, 16].

To overcome some of these problems, routines have been developed that seek to model the whole spectrum by fitting a background and cross-section shapes (e.g. Verbeeck *et al.* [17, 18]). However, background perturbations and uncertainties in the accuracy of the cross-sections remain. No information about the fine structure goes into the model, although the shape of the fine structure present can be fitted so that information about it is extracted.

Another approach is to use statistical methods to extract the information present [19, 20], as implemented in HyperSpy [21], for example. This is very powerful technique for extracting information from a large dataset and can pick up information that might otherwise be missed. However, the information still needs to be converted into physical quantities.

A third approach is to use standards. In an earlier paper, a method of extracting absolute energy differential cross-sections from standards is described [16]. This gives the absolute cross-sections for four binary standards, $TiC_{0.98}$, $TiN_{0.88}$, $VC_{0.83}$ and $VN_{0.97}$. In the current paper, these are used to quantify the (V,Ti)(C,N) precipitates that are used to increase the yield strength of high manganese steels being developed for automotive applications. More detail on the steels is given in our earlier paper [11]. The use of these cross-sections to quantify the experimental data is investigated with the aim of demonstrating the sensitivity and accuracy that can be achieved. The process uses multiple linear least squares (MLLS) fitting of the experimental cross-sections to the data. The fit coefficients allow the composition of the precipitates to be found. From the composition of the precipitate, its lattice parameter can be estimated e.g. using the data of Goldschmidt [22]. When the fit coefficients are normalised by the intensity of the zero-loss peak, the numbers of atoms per unit area are obtained. Since the number of atoms per unit volume is known from the lattice parameter, the precipitate thickness and volume can be found.

2. The Approaches to Quantification

For a single scattering distribution,

$$\frac{dI}{dE} = I_0 \sum_{elements\ i} \sum_{shells\ j} N_i \frac{d\sigma_{ij}}{dE} \tag{1}$$

where dI/dE is the intensity per unit energy at a given energy loss, I_0 is the intensity of the zero loss peak, N_i is the number of atoms per unit area (areal density) of the i^{th} element and $d\sigma_{ij}/dE$ is the partial cross section of an electron in the j^{th} shell of the i^{th} atom provided that it has a lower ionisation energy than the energy loss under consideration. The quantities dI/dE

and $d\sigma_{ij}/dE$ depend on the probe and collection half angles. Ideally, the data and the standards should be obtained on the same instrument using the same operating parameters. The reason for this requirement is that aberrations in the projector system can cause the collection half angle to change with energy loss [23].

Normalising the experimental spectrum by the zero loss intensity to give $(1/I_o)(dI/dE)$ gives a sum of the products of atoms per unit area and differential cross-sections. Quantification involves separating the terms in the sum and using cross-sections to give the atoms per unit area in the precipitate. In doing this, four things must be achieved:

1. Removal of the bulk and surface contributions arising from the matrix;
2. Dealing the background successfully;
3. Dealing with the differences in stoichiometry between the standards and the precipitate;
4. Making allowances for any non-idealities in the data.

3. Experimental Methods

Since the original paper on the extraction of the precipitate SI [11], both the instrumentation and the techniques have improved. The spectrometer has had hardware changes to lower the stray scattering and to reduce the defocus with energy loss. It has been realigned to improve the linearity of the dispersion. The set-up to minimise the stray scattering has been optimised as has the choice of the ratio of the high-loss to low-loss acquisition times (the time ratio) and the number of integrations per acquisition.

Since the precipitate data and the standards are recorded under the same conditions on the same instrument, chromatic effects in the projector system will have no effect on the quantification obtained using the standards. Investigation of these effects shows that a collection angle half angle at zero loss of 36 mrad only increases by 1% for a loss of 500 eV in the instrument used [23]. To use the experimental cross-sections on data recorded on other instruments, it is important to confirm that such chromatic effects are not significantly different in those instruments.

The precipitate data recorded in our original paper [11] has been re-acquired to take advantage of these improvements and make it as consistent as possible with the experimental

cross-sections [16]. The experimental conditions are summarised here. Further details can be found in the earlier papers.

The steel analysed is a high manganese steel of base composition in weight % is 20%Mn, 1.5%Al, 0.6%C (balance Fe) with an addition of 0.2% of V. It has a small and undetermined Ti content in the range 60-70 ppm from the original feedstock. The steel was held at 850 °C for 100 s and this gave precipitates with sizes in the 5 - 10 nm range. TEM lamellae are prepared using FIB lift-out, as described in the earlier paper [11]. To minimise carbon growth under the electron beam, the sample rod is cleaned for 3-5 minutes in a plasma cleaner prior to mounting the specimen, which is then plasma cleaned for a short time (typically 90 s)[1].

Areas containing precipitates suitable for spectrum imaging are identified from maps of the V $L_{2,3}$-edge using energy filtered electron microscopy with a Gatan GIF2000 on an FEI Tecnai T20 operated at 200 kV using either a LaB_6 or tungsten filament.

All SI datasets are recorded using a JEOL ARM200F operated at 200 kV and equipped with both a cold field emission gun as the electron source and a probe corrector. A Gatan 965 Quantum ER spectroscopy system with fast DualEELS is used for the recording of the SIs. They are recorded using the Digital Micrograph (2.x) software, with the scans under the control of Digiscan-2 hardware. For all SIs recorded in this work, a convergence half-angle of 29 mrad is used. The spot size is ~1 Å and the condenser setting is chosen to give a probe current in the range 180 to 400 pA. For EELS, the camera length is chosen so that the 2.5 mm aperture of the Quantum gives a collection half-angle of 36 mrad, resulting in high collection efficiency. A dispersion of 0.5 eV per channel is used. Typically a time ratio of 25 and a splice point of ~100 eV are used. This choice of splice point determines the energy offset required for the high-loss spectrum, which, in turn, determines its integration time so that the signal remains in the linear region of the CCD (below about 50,000 counts per pixel for our Ultrascan). The integration time for the low-loss is set by the requirement to keep the zero-loss peak in the linear range of the CCD (as above).

Typically, there are 5 integrations per spectra with an integration time of 200 μs for the low-loss and 5 ms for the high-loss. With the readout overheads, this gives a recording time

[1] This procedure differs from that used for the binary standards, where minimisation of surface oxidation was the aim. However, the steels undergo surface oxidation rapidly after the FIB thinning and plasma cleaning does not seem to alter this. Thus plasma cleaning is used to minimise carbon contamination.

of ~110 ms per pixel in the SI. With these experimental conditions, the standard splice routine in DigitalMicrograph can be used with a 20 channel overlap to splice the spectra. A map of the splice ratio at each pixel can be extracted. Regions with mean values of t/λ in the range ~0.15 to ~0.43 are used for the datasets analysed below. All data are recorded without orienting the specimens to specific diffraction conditions. Thus it is assumed that strong channelling effects are not present in the data. In any case, these would be relatively small due to the large probe and collection angles [16].

4. Quantifying the Data

4.1. The Single Scattering Distribution

The datasets are processed to give single scattering distributions for the whole energy range. The procedure used is described in the earlier papers [11, 16]. In summary, the spectra in the low-loss and high-loss dataset are aligned in energy using the zero loss peak, any x-ray spikes larger than 5σ are removed, channels containing no useful information are removed at either end of the spectra, and principal component analysis (PCA) is used for noise reduction using the plug-in for Digital Micrograph developed by Lucas *et al.* [24]. The spectra are then spliced and Fourier-log deconvolved to give the single scattering distributions.

4.2. The Surface Oxide and the Bulk Matrix

In the initial paper [1], the precipitate SI is "extracted" from the single scattering on the assumption that there is no Fe in the precipitate. To do this, the "average matrix" spectrum is obtained from pixels outside the projected position of the precipitate. At each pixel, the "average matrix" spectrum is scaled so that its Fe $L_{2,3}$ intensity matches that in the spectrum at the pixel. It is then subtracted to remove the matrix contribution, leaving only the signal from the precipitate. However, this process does not deal correctly with effects of the surface layers that are present. Evidence from diffraction and dark field imaging suggests that there are coherent, thin layers of iron oxide on the surfaces and that this oxide is likely to be based on the magnetite structure, Fe_3O_4 [25]. The intensity of the O K-edge in the matrix regions suggests that the thickness of the oxide layers is constant over much of the specimen. However, the oxide layers could contain contributions from the other alloying elements present in the steel including C, which is present at 0.6 wt.% or 2.7 at.% according to the bulk composition. With the cleaning procedures described the previous section, there is little or no evidence of additional layers of amorphous carbon (a-C) "contamination" induced by the electron beam although, as shown below, it is present in very localised regions.

The "average matrix" spectrum used in the initial paper [11] actually contains a contribution from both the bulk and surface of the matrix. For the ideal case of a precipitate contained within a lamella of constant thickness, the surface layer has a constant thickness in each pixel but the thickness of the matrix will decrease in those pixels in which the precipitate is present. Thus, in such pixels, the process of scaling and subtracting the "average matrix" spectrum using the Fe $L_{2,3}$ intensity causes a reduction in the amount of the surface contribution subtracted. This leaves some K-edge contributions from the O K-edge, which may interfere with the quantification.

Thus a better method of making a correction for the surface layers is required. Two approaches are compared here. The first investigates separating the bulk and surface signals so they can be used separately. The second uses two average matrix spectra from regions in the SI with different values of t/λ.

For a single scattering distribution, t/λ and $(1/I\mathrm{o})/(dI/dE)$ can be expressed as sums of bulk (B) and surface (S) contributions:

$$\frac{t}{\lambda} = \left(\frac{t}{\lambda}\right)_B + \left(\frac{t}{\lambda}\right)_S \tag{2}$$

and

$$\frac{1}{I_o}\frac{dI}{dE} = \left(\frac{1}{I_o}\frac{dI}{dE}\right)_B + \left(\frac{1}{I_o}\frac{dI}{dE}\right)_S \tag{3}$$

Following the approach used to give the experimental cross-sections, the slope of a plot of $(1/I_o)/(dI/dE)$ versus t/λ gives the bulk contribution per unit t/λ if the surface contributions are constant [16]. Thus the bulk contribution in a spectrum at a given t/λ is this slope multiplied by $(t/\lambda - (t/\lambda)_S)$. This bulk contribution can be subtracted from the actual spectrum to give the surface contribution. While $(t/\lambda)_S$ is not known, it should have a fixed value if the surface layer is uniform. Thus the value of $(t/\lambda)_S$ that gives the same surface contribution from spectra with different values of t/λ is the correct value.

Figures 1a and b show the average contribution from the surface layers in the low-loss and core-low regions respectively. They are obtained using data from three regions with different values of t/λ. The deviations from the average of the contributions obtained from each dataset are also shown. These are small with fractional deviations of less than 2% except at energy losses below ~12 eV where they rise. This confirms that the surface layer

on the matrix is uniform to a good approximation in these three regions. The value of $(t/\lambda)_S$ giving the best agreement is 0.10.

Figures 1c and 1d show the surface and bulk contributions from the specimen with an average matrix t/λ of 0.149 (Precipitate 1 below) in the low-loss and core-loss regions respectively. They also compare their sum to the original spectrum demonstrating excellent agreement.

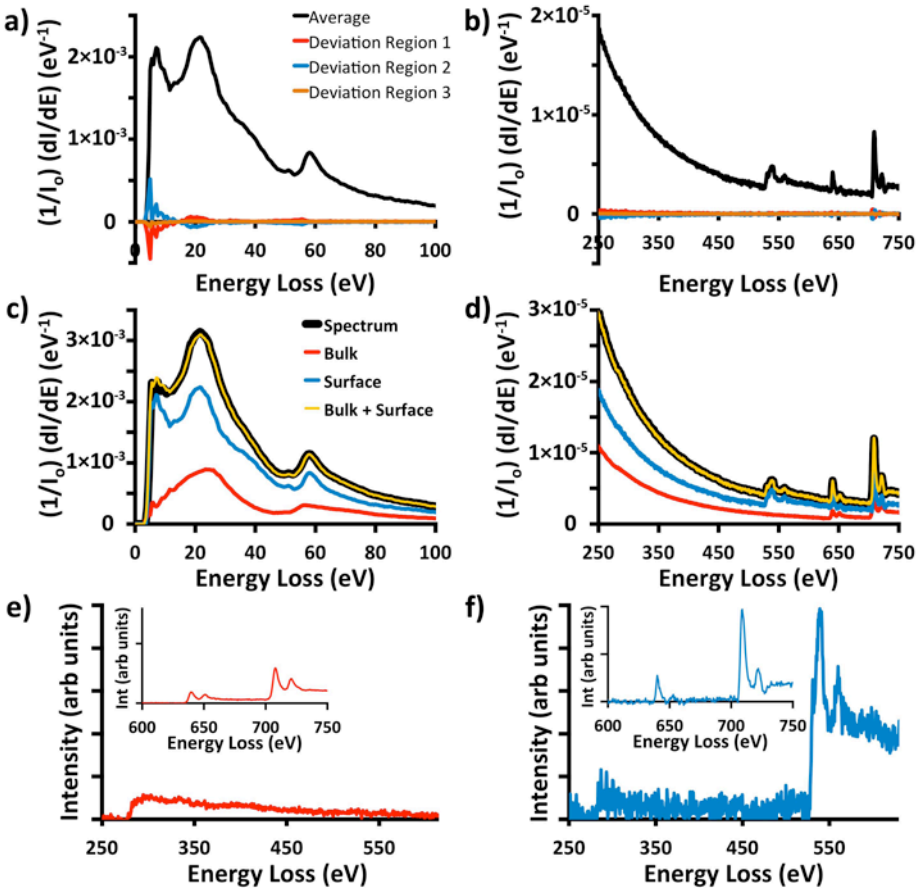

Figure 1. a) The average surface layer contribution and the deviations from it in the low loss region. b) The same in the core-loss region. c) The contributions of the surface and bulk to the low loss spectrum in the thinnest region. d) The same in the core loss region. e) The bulk contribution after subtraction of a power law background fitted in the window from 245 to 270 eV. The inset shows the Mn and Fe $L_{2,3}$-edges on an expanded vertical scale after background subtraction using window from 593 to 693 eV. f) The surface contribution after background subtraction using the 245 to 270 eV window. It has been scaled to have the same same C K-edge intensity over 290 to 310 eV. The inset shows the Mn and Fe $L_{2,3}$-edges. The relative scaling between the insets is the same as that in the main figures.

Figures 1e and f show the regions containing the C and O K-edges for the bulk and surface contributions after subtraction of a power law background fitted in a window from 245 to 270 eV. They are scaled to have equal intensities in the window on the C K-edge from 290 to 310 eV. The insets show the corresponding Mn and Fe $L_{2,3}$-edges after background subtraction using a window from 593 to 633 eV. The relative scaling is the same as that for the C K-edges in the main figures.

Figure 1e shows that there is no O K-edge from the bulk, as expected. However, there is a significant C K-edge. Its shape is not that of amorphous carbon. This is to be expected since the surface contributions have been removed. Thus this C K-edge comes from the 0.6 wt.% (2.7 at.%) C content of the matrix. It shows no significant ELNES unlike the C edges in the precipitates or the binary standards. However, it makes a significant contribution to the C K-edge signal in the precipitate region and must be separated from the contribution from the precipitate itself.

An estimate of the bulk composition using the traditional quantification method [15] gives 7.6 at.% C, 20.8 at.% Mn and 71.6 at.% Fe. From the bulk composition, the corresponding values are 2.8 at.% C, 20.4 at.% Mn and 77.1 at.% Fe. The metal fractions are in moderate agreement but there is a significant difference in the values for carbon. Background fitting before the C K-edge requires judgment because of the EXELFS but the shape of the extracted edge is reasonable. Thus it is not clear why the EELS value exceeds the bulk value when any surface carbon should have been removed.

The C K-edge from the surface is shown in Figure 1f and is scaled to have the same intensity as that in the bulk. The noise level is such that it is not possible to tell from the ELNES whether it is in the form of a-C or C from the matrix incorporated in the oxide, which is possible. The O K-edge is much more intense, as would be expected from a structure based on Fe_3O_4. Comparison of the insets also shows that the Fe to Mn intensity ratio is far higher in the oxide. The estimate of the composition from the traditional quantification method gives 2.5 at.% C, 52.5 at.% O, 4.4 at.% Mn and 40.6 at.% Fe, which is certainly consistent with $(Fe,Mn)_3O_4$. Assuming the C is incorporated in the oxide, the value of the (C+O)/(Mn+Fe) ratio is 1.2 which is also in the correct range for an oxide based on Fe_3O_4. If the C is in the form of a-C on the surface, it is present as a very thin layers with a total thickness ~1 nm.

The shape of the O K-edge also shows the type of ELNES expected from bonding between O and Fe/Mn. Comparison of the inset Fe and Mn $L_{2,3}$-edges shows that the ratios of the L_3 to L_2 white line heights are far larger in the oxide than in the matrix for both elements. This is expected for the Fe edge [26, 27] and also appears to be the case for Mn, at least going from metal to Mn^{2+} [28]. These results show that the combined effect of the FIB milling and the subsequent oxidation is not simply adding O while keeping the ratios of the matrix elements constant. While interesting in itself, investigation of the oxidation process lies outside the scope of this paper.

Since the oxide layer has a well defined $(t/\lambda)_S$, it would seem that the surface oxide layer can be removed from the spectrum image by a simple subtraction if the latter is normalised by I_o. However, the problem is more complicated. There is some evidence that the oxide thickness can differ from region to region. In addition, given that $(t/\lambda)_S$ is ~0.1 and t/λ is in the range 0.15 to 0.43, it is likely that some precipitates were at or close to the surface of the as-thinned lamellae and the oxidation process may be modified in such cases.

If the oxide thickness varies from region to region, dealing with it becomes similar to dealing with the bulk matrix. For the bulk matrix, it is possible to scale the bulk matrix contribution using the intensity of the Fe $L_{2,3}$-edge, as described in the earlier paper [11]. However, for the removal of the surface oxide contribution, it is not straightforward to extract the O K-edge intensity in the presence of the precipitate because of the overlap with the V $L_{2,3}$-edge.

An alternative way forward is to include the shapes of the surface and bulk contributions in an MLLS fit, as described below. However, issues arise with the background levels in the resulting maps and these issues are discussed in more detail below. A more robust result is obtained if use is made of the thickness variations of the matrix present in the SIs. For each SI, an average shape is taken in the thinnest matrix region and another one in the thickest. These represent two linear combinations of the bulk and surface contributions. In principle, a linear combination of the contributions from the thin and thick matrix will give the shape of any other combination of bulk and surface contributions. However, the changes of t/λ over the small fields of view are small (~0.017) and so there may still be issues in the region of the precipitate. Nonetheless, it is shown below that the O K-edge signal is removed effectively if these two matrix shapes are used in the MLLS fit instead of the bulk and surface shapes.

4.3. The Background

Dealing with backgrounds under the edges is the most challenging part of quantifying EELS data. The earlier papers [11, 16] show that the background from the matrix has significant deviations from a simple power law shape. These deviations arise from EXELFS from lower lying edges. Thus subtracting backgrounds from the steel data and the standards data before attempting quantification is a potential source of significant error.

An alternative approach is to make an MLLS fit to the deconvoluted but non-background-subtracted steel data using vanadium and titanium carbide fit components that are also non-background-subtracted (vanadium nitride could also be added but this simply adds complexity to the fit when the N is a minor constituent in the precipitates examined in this work). However, stoichiometric C and N standards (from carbides and nitrides) are required to allow for changes in stoichiometry between the binary standards and the precipitate. Background subtraction is an integral part of obtaining these standards [11, 16] and so they must be used with the background subtracted. To allow for this, the background shape used to extract these C and N shapes for carbide and nitride must be included in the fit as another component.

Figure 2a shows the result of such a fit for the precipitate in a region with an average matrix t/λ of 0.259 (Precipitate 2 below). The corresponding fits for the other three precipitates are shown in Figure S1 of the Supplementary Material. The components used in the fit are discussed further in §4.4. The spectrum shown is summed over a 6 x 6 pixel region in the centre of a precipitate and compared to the MLLS fit and the residuals (shown multiplied by 5). The fit is made over the energy range from 150 to 750 eV and the residuals are small except in the vicinity of the edge thresholds and in the 150 to 200 eV range. While those in the 150 to 200 eV range are significant in absolute terms they are the smallest in fractional terms. The most likely explanation for them is the presence of small changes in the EXELFS arising from the alloying of TiC and VC, and from the interface between the precipitate and the matrix. Those at the edge thresholds are likely to be due to sub-channel misalignments in energy and slight changes in the ELNES on the edges of the elements in the precipitates due to changes in composition relative to the standards.

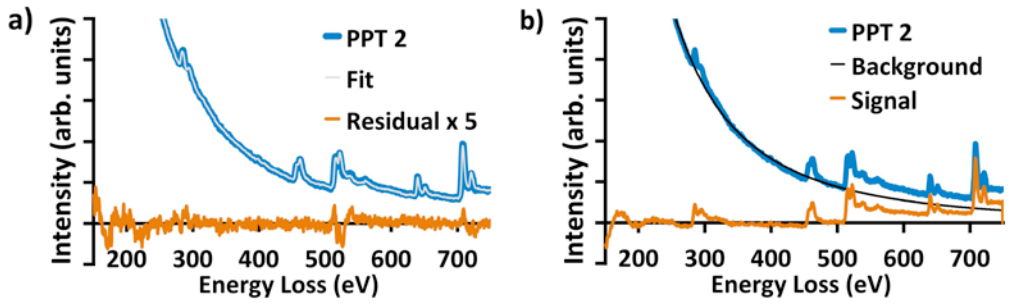

Figure 2 The spectrum from Precipitate 2 summed over 6x6 pixels in its centre. a) An MLLS fit over the range 150 to 750 eV and the residuals multiplied by 5. b) A power law background fitted over the range 150 to 280 eV and the resulting background subtracted signal.

The result of a power background fit over the energy window from 150 to 280 eV is shown in Figure 2b. The background does not fit well at the start of the window and the deviations of the signal from zero prior to the C K-edge are more extensive and much bigger than the residuals in the MLLS fit. In addition, the background extrapolation cuts through the data ~50 eV beyond the C K-edge. Figure 2b clearly illustrates the background subtraction issue when using a power law background while Figure 2a shows that a much better fit to the background is obtained using an MLLS fit without background subtraction.

4.4. Components Included in the MLLS fits

In addition to the components mentioned above, three other components are included in the fit. One is the deconvolved, background subtracted C K-edge shape from an a-C film. This is required because, when fitting to some of the precipitates, the electron loss near edge structure (ELNES) on the C K-edge is not fitted well using the $VC_{0.83}$ and $TiC_{0.98}$ experimental cross-sections alone. The residuals indicate a contribution from a-C.

The other two components are minor artefacts associated with dark current subtraction. One is simply a constant to take account of slight errors in the overall dark current levels subtracted from the various datasets. If it is not included, the fit can sit slightly high or low with respect to the data. The other takes account of slight differences in the dark current subtraction that can arise between the two quadrants of the CCD used to read out the high loss

spectrum[2]. This effect results in an intensity step at the central channel of the original high-loss spectrum and the step height and sign vary from pixel to pixel. An example of such a step can be seen in Figure 3. Thus a step function component, which is zero up to the energy loss at which the step occurs and unity after, is included in the fit. The residuals (shown x5) show that the fit is excellent over the spectrum, confirming the artefact is a constant offset. The contribution to the fit from this step function component is given by its product with its fit coefficient. Subtracting this contribution from the SI removes the step artefact, as shown in Figure 3.

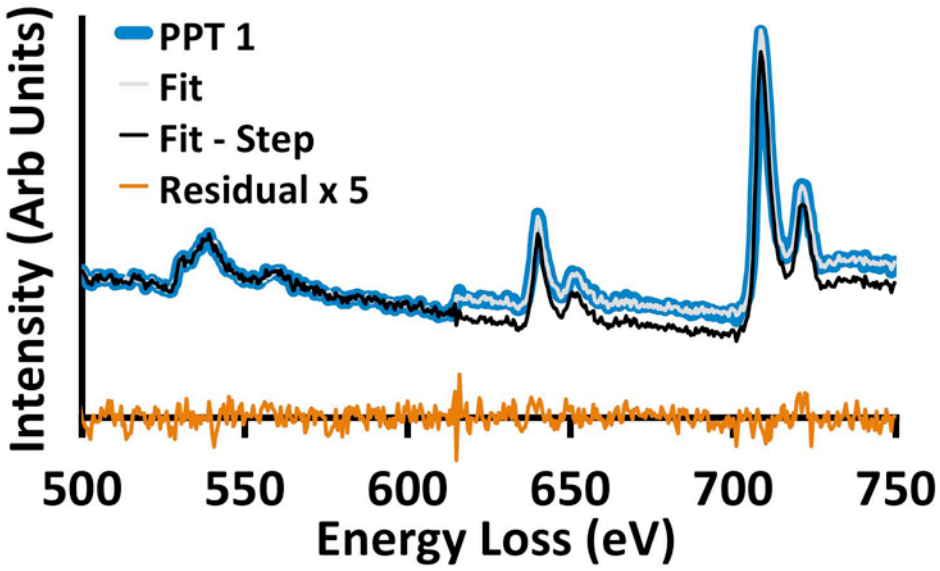

Figure 3 Spectrum from a single pixel showing the step caused by the difference in the dark current subtraction in two quadrants of the UltraScan camera. Also shown is the MLLS fit when a step function is included, the residuals (x5) and the result after subtracting the contribution of the step function.

In summary, the components used in the MLLS fit are:

a. shapes from thick and thin matrix regions or from the bulk and surface contributions from the matrix;
b. the binary experimental cross-sections for $VC_{0.83}$ and $TiC_{0.98}$ as the largest contributions to the precipitate composition;

[2] The CCD camera has four quadrants which are read out independently. The upper two are used for the high loss spectra and the lower two for the low loss spectra. A similar problem will arise in the low loss data. However, in the processing scheme used here, only data from one of the low loss quadrants is spliced to the high loss data. Thus any step in the low-loss data is not present in the spliced SI.

c. the background subtracted, stoichiometric experimental cross-sections for the C K-edge (from $VC_{0.83}$) and the N K-edge (from $VN_{0.97}$) to allow for changes of stoichiometry between the precipitate and the binary standards;
d. the background shape used to extract the C and N cross-sections to provide the background missing from the these cross-sections;
e. the C K-edge shape from a-C to allow for its possible presence;
f. the constant and the step function shapes to allow for the dark current artefacts.

In all, there are a total of 10 components in the fit. It is possible to add more e.g. the background subtracted C K-edge cross-section from $TiC_{0.98}$ in order to try to further improve the fit to the C K-edge ELNES or the binary experimental cross-section from $VN_{0.97}$ to improve the fit to the V $L_{2,3}$ white lines. While the former shows little improvement, the latter shows a significant improvement. However, the changes in the resulting quantification are minor in both cases. Thus, for simplicity, only the fits using 10 components listed above are used here.

A word of caution is worthwhile here. The MLLS fitting routine in Digital Micrograph v2.x can be subject to rounding errors if the magnitudes of the components differ by too large a factor. Thus those components that provide only shapes rather than absolute values should be scaled so that their magnitudes are similar to those with absolute values.

4.5. Using The Fit Coefficients To Quantify The Precipitates

The results of the MLLS fit using the components described in the previous section are ten maps of the fit coefficients for these components plus a map of the sum of the square deviations for the fit at each pixel and two SIs, the fit to the spectrum at each pixel and the corresponding residuals i.e. deviations of the data from the fit.

The precipitates are characterized by the fit coefficients for the four components in groups b and c of the list of components in the previous section i.e. $b_{VC_{0.83}}, b_{TiC_{0.98}}, b_C, b_N$.

Such a fit coefficient is the contribution of the corresponding component of the spectrum intensity, I_i, divided by its differential cross-section. Based on the same argument that gives Equation (1) and taking $I_i = (dI_i/dE)\Delta E$ where ΔE is the channel width, each coefficient, b_i, is given by:

$$b_i = I_0 \, N_i \, \Delta E = I_0 \, n_i \, t_i \Delta E \quad (4)$$

where I_o is obtained from the low loss data, after correction for the difference between the time ratio and the splice ratio as discussed in the earlier papers [11, 16], N_i is the number of formula units of the component per unit area, n_i is the number of formula units per unit volume and t_i is the thickness of the component along the beam (see below).

Thus $b_{VC_{0.83}}$ and $b_{TiC_{0.98}}$ are proportional to the number of V and Ti atoms per unit area respectively while their sum is proportional the total number of metal atoms per unit area. The sum $\left(0.83b_{VC_{0.83}}+0.98b_{TiC_{0.98}} + b_C\right)$ is proportional to the number of C atoms per unit area while b_N is proportional to the number of N atoms per unit area. Since I_o and ΔE are common, the values of x, y and z in the formula $Ti_xV_{(1-x)}C_yN_z$ can be found pixel by pixel e.g. $x = b_{TiC_{0.98}}/\left(b_{VC_{0.83}}+b_{TiC_{0.98}}\right)$. As the signal from the precipitate decreases towards the edge, as well as in regions where there is no signal from the precipitate, noise dominates these values, and this is considered further in §5.5 below.

The precipitates of interest here have the cubic rock salt structure or a small distortion of it [22, 29, 30]. Once the composition is determined, the lattice parameter can be interpolated from published data e.g. Goldschmidt [22]. Hence the number of metal sub-lattice sites per unit volume can be found. This is equal to the number of non-metal sub-lattice sites per unit volume in this structure. Assuming that all the metal sites are occupied, the precipitate thickness can be calculated from $\left(b_{VC_{0.83}} + b_{TiC_{0.98}}\right)$ together with the values of I_o and ΔE. Partial thicknesses for the four elements can also be calculated using Equation (4) when n_i is taken as the number of sub-lattice sites per unit volume i.e. by assuming an element fills all its sub-lattice sites

5. Results

The above methodology has been applied to four precipitates in the same FIB lamella. Precipitates 1, 2, 3 and 4 are in regions where the matrix has mean values of t/λ of 0.149, 0.259, 0.315 and 0.425 respectively.

5.1. Comparison of the Fit Coefficient Maps

Figure 4 compares the fit coefficient maps of the $VC_{0.83}$, $TiC_{0.98}$, stoichiometric C (from $VC_{0.83}$), stoichiometric N (from $VN_{0.97}$) and a-C components for the four precipitates. The maps for the other fit coefficients are shown in Figure S2 of the supplementary material.

In the matrix regions, the values of these coefficients are close to zero. Thus the matrix shows as "dark" in most of the maps. The exceptions are the maps for C from $VC_{0.83}$ where the coefficients are negative in the precipitate regions. Hence the matrix shows as "bright". Scales are not given for the intensities since the quantitative interpretation is given below.

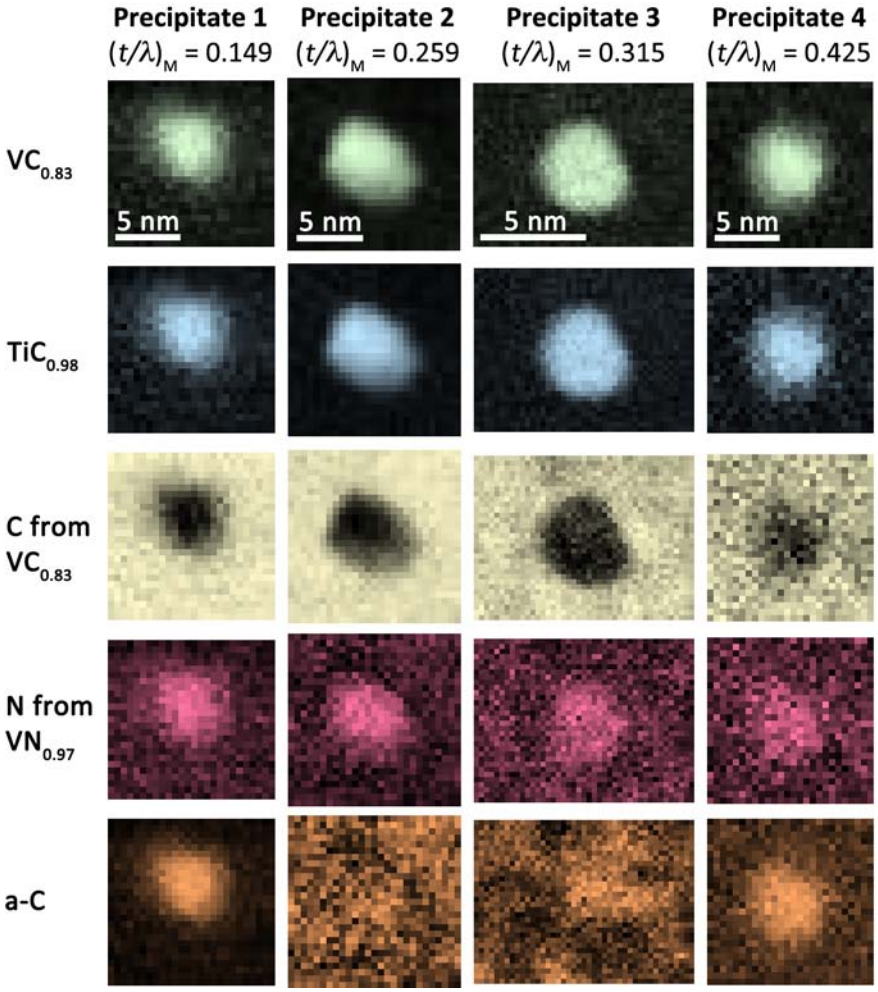

Figure 4. Maps of the fit coefficients for $VC_{0.83}$, $TiC_{0.98}$, stoichiometric C from $VC_{0.83}$, stoichiometric N from $VN_{0.97}$ and a-C (rows) for the four precipitates (columns). All the maps have the same scale. With the exception of the maps for C from $VC_{0.83}$, dark corresponds to a coefficent close to zero. For C from $VC_{0.83}$, the coefficient is negative in the precipitate region and so bright corresponds to a coefficient close to zero.

The maps for $VC_{0.83}$ and $TiC_{0.98}$ show the precipitates clearly The negative values of the coefficients of C from $VC_{0.83}$ in the regions of the precipitates show that the precipitates have less C than the combination of the two binary standards. The maps for N show a clear contribution for N in the precipitates but are much noisier than the other maps.

The maps for a-C show that there are significant contributions from a-C associated with Precipitates 1 and 4 but not with the other two. For Precipitate 3, the dark parts of the map correspond to a coefficient close to zero while the bright regions correspond to a coefficient midway between the peak values in the maps for Precipitates 1 and 4. However, these regions do not correlate with the precipitate position.

5.2. Comparison of the Contributions to the Fits

It is difficult to quantitatively understand the contributions to the data made by each of the components from the maps in Figure 4 and S1. Figure 5a and b compare the contributions to spectra summed over 6x6 pixel regions in the centres of the precipitates for Precipitates 1 and 2 respectively. Only the contributions from eight components of the fit and the fit residuals are shown. The two contributions from the matrix are not shown so that the small contributions can be seen clearly. To give an indication of the sizes of the matrix contributions, the intensity of the spectrum at an energy loss of 250 eV in Figure 5a is 1.2 times the height of the vertical axis and that in Figure 5b is 1.5 times.

The contributions from the precipitate components are smaller in Precipitate 1 than 2. However, the contribution of a-C is much higher and well above the noise in the residuals whereas that in Precipitate 2 is at the level of the noise in the residuals. There is a net positive contribution from the background-subtracted components for Precipitate 1 and a corresponding positive contribution from the background component. However, the net contribution from the background subtracted components for Precipitate 2 is negative which should lead to a negative background contribution but it is actually positive. Thus the background term appears to be compensating for some other effect as well.

The step function and constant contributions have magnitudes similar to the peak-to-peak noise in the residuals and so their values are in keeping with the reasons for their inclusion. For all four precipitates, a correlation of the size of the coefficient of the constant component with precipitate position can be seen in Figure S2. This is to be expected if precipitate components have slightly different offsets to the matrix components since the coefficient will depend on the relative contributions in a given pixel.

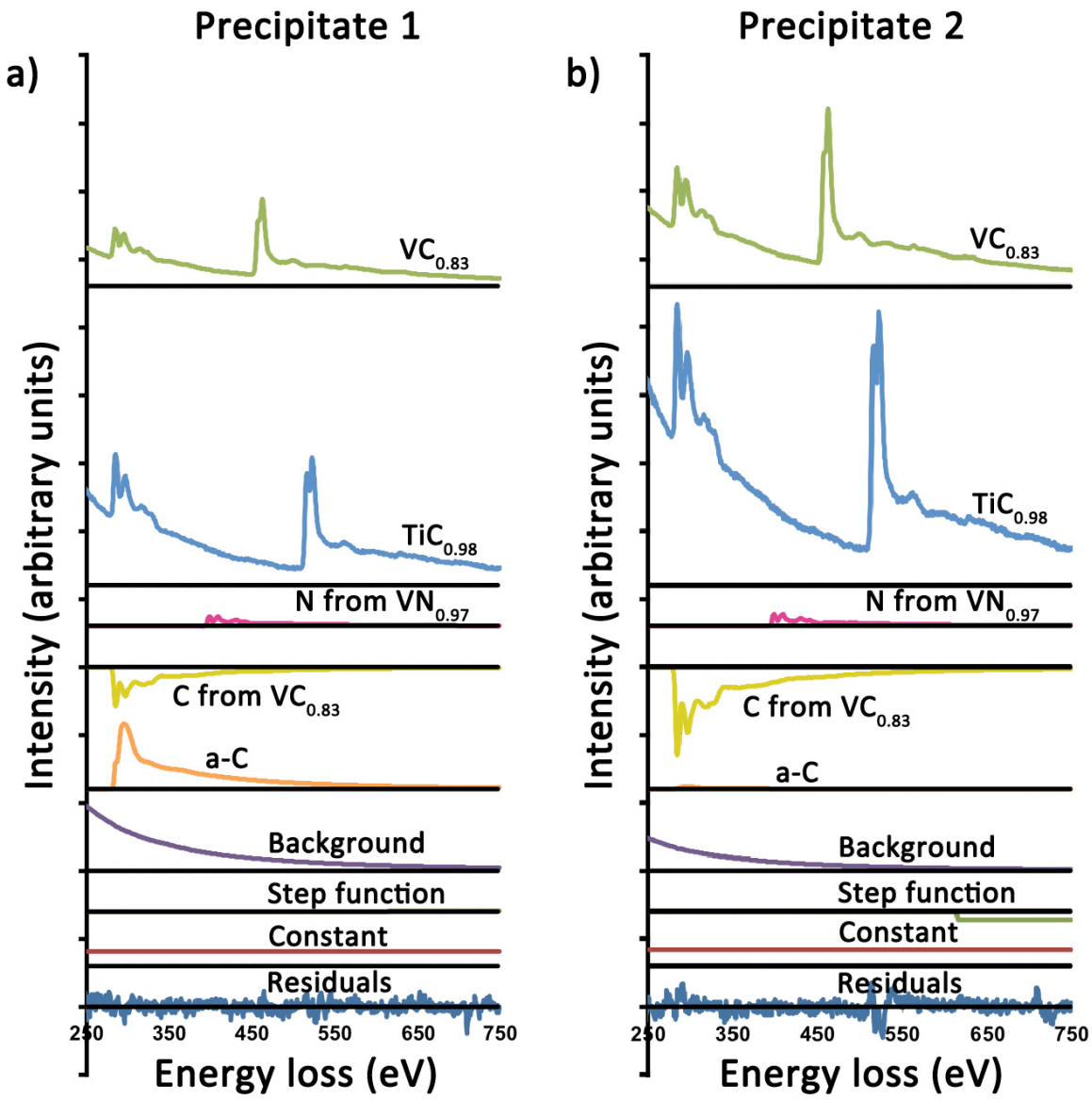

Figure 5. a) The contributions of the components to the fit to Precipitate 1 in a spectrum summed over 6x6 pixels in the centre. The matrix contributions are not shown. At 250 eV, the total spectrum intensity is ~1.2 times the height of the vertical scale. b) The same for Precipitate 2. The vertical axis has the same scale as that in a) but the total spectrum intensity at 250 eV is ~1.5 times its height..

At this point, checks can be made on how successfully the surface oxide is removed from the precipitate data and on how well the C K-edge of the precipitate is extracted. The results presented use thin and thick matrix contributions in the fit. Figure 6a to d compare spectra summed in a 6x6 pixel regions in the centres of the four precipitates.

Figure 6a shows the spectra from the deconvolved SIs background subtracted using a window from 477 to 507 eV[3]. Also shown is the V $L_{2,3}$-edge from the experimental $VC_{0.83}$ cross-section. This contains no O K-edge signal and is used as a reference. The V $L_{2,3}$-edges prior to the O K-edge threshold are scaled so that the integrated counts are the same. In Figure 6a, the spectra from all the precipitate show very significant contributions from the O K-edge due to the surface oxide on the matrix.

Figure 6b shows the same spectra after removal of the contributions from the thin matrix, the thick matrix and the a-C. The V $L_{2,3}$-edges from the precipitates now follow closely that from the binary $VC_{0.83}$ experimental cross-section, showing excellent removal of the O K-edge contributions.

Figures 6c and d show the equivalent results for the C K-edge after background subtraction using a window from 245 to 270 eV. The C K-edge from the $VC_{0.83}$ experimental cross-section is used as the reference and the edges are scaled to the same intensity over the energy range 300 to 340 eV. In Figure 6c, the ELNES changes markedly from precipitate to precipitate and differs significantly from that of the C K-edge from $VC_{0.83}$. After subtraction of the matrix and a-C contributions, Figure 6d shows the C K-edge shapes are now in much better agreement with that from the $VC_{0.83}$ reference despite the noise. The increasing divergence at higher energy loss is the result the problems arising from the use of a power law background, as discussed above.

[3] The background window for Precipitate 1 in Figure 6b had to be changed to 498 to 511 eV because of a perturbation to the background shape in front of the edge.

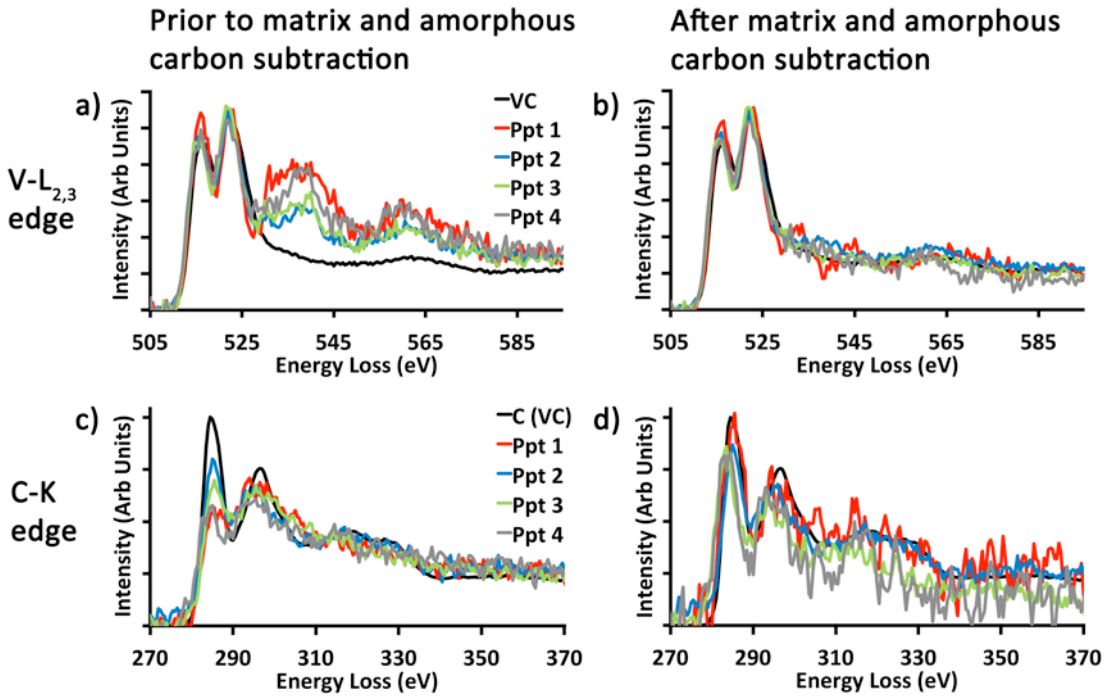

Figure 6 a) V $L_{2,3}$-edges from the four precipitates compared to that from the $VC_{0.83}$ experimental cross-section after background subtraction using a fitting window from 477 to 507 eV (498 to 511 eV for Precipitate 1). b) The equivalent spectra after the matrix and a-C contributions from the MLLS fit have been subtracted. c) C K-edges from the four precipitates compared to that from the $VC_{0.83}$ experimental cross-section after background subtraction using a fitting window from 245 to 270 eV. d) The equivalent spectra after the matrix and a-C contributions from the MLLS fit have been subtracted. The spectra are taken from 6x6 pixel regions in the centres of the precipitates. For a) and b), the V edges are scaled to the same intensity in the region prior to the O K-edge threshold. For c) and d), the edges are scaled to the same intensity from 300 to 340 eV.

5.3. Comparison of the Partial Thickness Profiles of the Precipitates

The partial thicknesses of V, Ti, C and N are calculated using the method given in §4.5. Line profiles of these partial thicknesses through the centres of the precipitates are shown in Figure 7. These line profiles are one pixel wide and run from top to bottom on the maps in Figure 4. Three profiles are shown in each case. For the solid black profiles, the fit uses thin and thick matrix components extracted from the individual spliced, deconvolved SIs. The fitting region is from 150 eV to 750 eV and the fits are shown in Figures 2 and S1. The other two traces use the bulk and surface shapes, described in §4.2, as the matrix components.

For the red profiles, the fitting region is 150 to 750 eV, where the fit in the region from 150 to 250 eV is not good. For the dotted blue profiles, the fitting region is 200 to 750 eV, which results in better fits over this region.

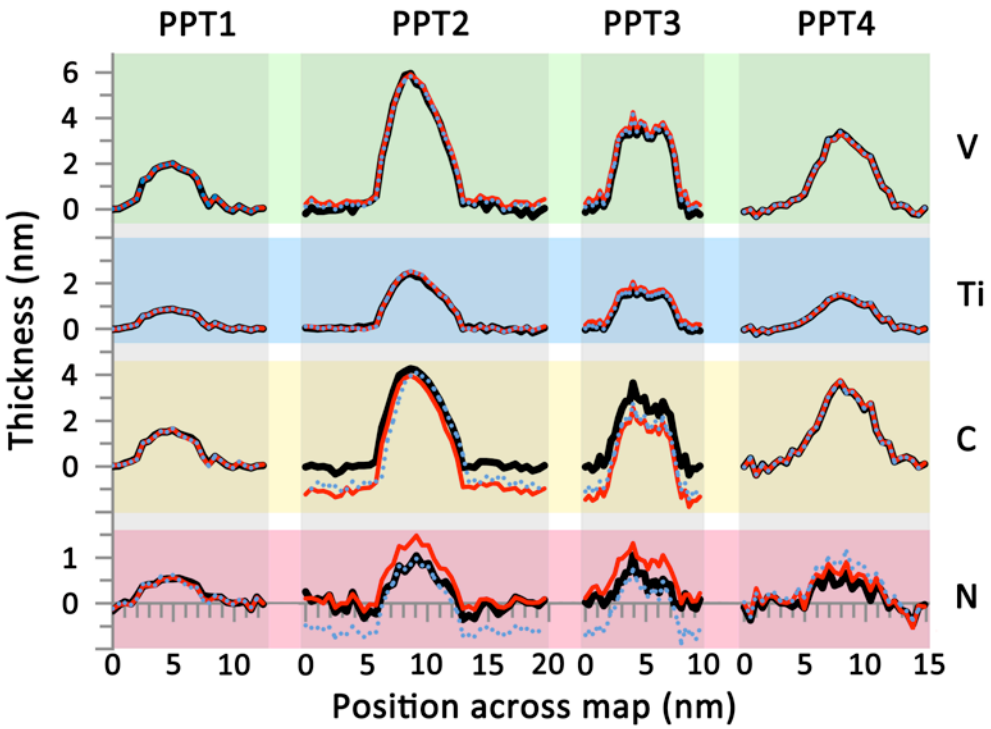

Figure 7. Vertical line profiles of the partial thicknesses of the four elements in the four precipitates (note the expanded vertical scale for N). The profiles are 1 pixel wide and taken through the centres of the precipitates. The results for three MLLS fits are shown. The black solid lines use thin and thick matrix components and the fit is over the range 150 to 750 eV. The red lines use bulk and surface components and the fit is over 150 to 750 eV. The blue dotted lines use bulk and surface components and the fit is over 200 to 750 eV.

For V and Ti, which give the largest signals, the profiles from the three fits are in good agreement. In the case of the Precipitate 3, the profiles using the bulk and surface component have small offsets from zero in regions where there is only matrix but the thickness within the precipitate is unaffected. A similar offset is present in the C profiles from Precipitates 2 and 3 but the thickness within the precipitate is also affected for Precipitate 3. The offsets for the N profiles are worse and the thicknesses of Precipitates 2, 3 and 4 are all affected. However, for all four precipitates and for all four elements, the profiles obtained using the thin/thick matrix components lie close to zero in the regions where there is only matrix. This is the justification for the earlier statement that the use of the thin/thick matrix components results

in more robust fits. Hence only results from fits using these components are considered further below.

For a given precipitate, the profile shapes are very similar for all four elements showing that the composition is relatively homogeneous and the homogeneity will be considered in more detail in §5.5 below. The N partial thickness is by far the lowest and Figure 2 shows that the N K-edge intensity is very weak. Thus a necessary cross-check is to verify that there is a measurable N K-edge signal in the original data and that it is not an artefact introduced by the PCA noise reduction procedure. Thus the as-recorded low-loss and high-loss SIs, after energy alignment and x-ray spike removal, are spliced and deconvolved. The same MLLS fits are then performed and vertical profiles are taken through the resulting N coefficient maps. Since these maps are much noisier, the profiles are averaged over a width of 7 pixels. Figure 8 compares these profiles (dashed green) with the equivalent ones after PCA noise reduction (solid black). For Precipitates 1, 2 and 3, there is excellent agreement in the overall profile shape but, as expected, the noise in the profiles without PCA is much greater. Thus the N signal in these three precipitates is real and not a PCA artefact. However, for Precipitate 4, which is in the region with the thickest matrix, the profile obtained without using PCA does not show evidence of the presence of N owing to the level of noise present. Nonetheless, the results from the data that has undergone PCA noise reduction are entirely in line with the results from the other three precipitates and so are presented below.

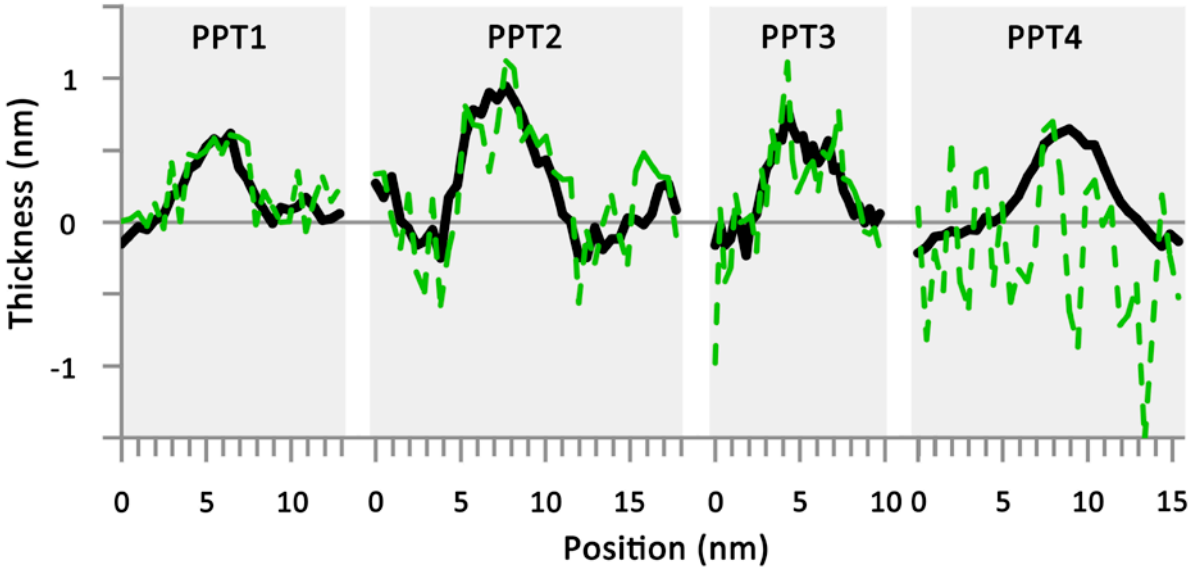

Figure 8 Comparison of the N partial thicknesses with (solid black) and without (dashed green) PCA noise reduction. The profiles are taken through the centres of the precipitates and are averaged over a width of 7 pixels.

5.4. Precipitate Thickness

One way of calculating the projected precipitate thickness is to add the partial thicknesses from Ti and V. The other is to measure the values of t/λ from the deconvolved SI after the matrix and a-C contributions have been subtracted. These values of t/λ can then be converted to thicknesses using the mean free path for the precipitate. This mean free path can be calculated from the Iakoubovskii parameterisation [31] after correction by the (80%) factor found in the previous paper [16]. Since this mean free path is equivalent to those used to calculate the experimental cross-sections, the thickness obtained by the two methods should ideally agree.

Figure 9 shows single pixel wide vertical line profiles of the thicknesses taken through the centres of the precipitates. For each precipitate, the purple solid line shows the thickness obtained from the sum of the Ti and V partial thicknesses and the dashed orange and dotted green profiles show the thicknesses obtained from t/λ. For the orange dashed set, only the thin and thick matrix contributions have been subtracted from the deconvolved SI while, for the green dotted set, the contribution from the a-C has also been subtracted. Precipitate 2 shows no change in thickness between the two sets. Precipitates 1 and 4 show systematic decreases in thickness, with maximum changes of 0.9 and 0.5 nm respectively. Such changes are expected since these precipitates show a clear a-C contribution associated with the position of the precipitate. Precipitate 3 shows a maximum change of ~0.9 nm but only on the side of the profile. This side of the profile corresponds to the bright region at the top of the a-C coefficient map for Precipitate 3 in Figure 4. Here the values of the coefficient are certainly higher but they are not obviously correlated with the precipitate position. Overall, the small changes in the thickness caused by subtracting the contribution from a-C confirm the low level of a-C present on the lamella.

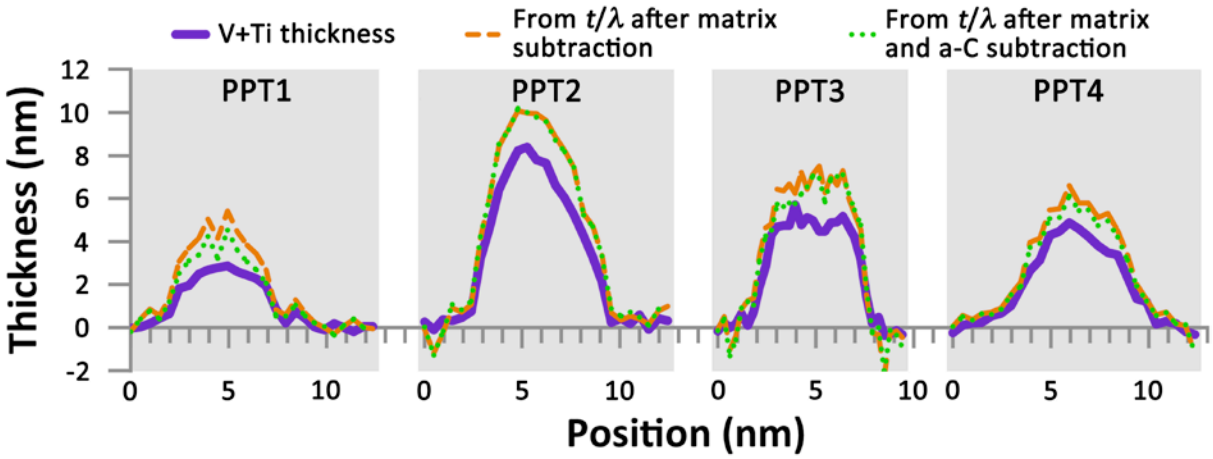

Figure 9 Comparison of the thickness profile of the four precipitates: from Ti+V (solid purple); from t/λ after subtracting the thin and thick matrix contributions (dashed orange); from t/λ after after additionally subtracting a-C contributions (dotted green). The profiles are taken through the centres of the precipitates and are 1 pixel wide.

For all four precipitates, the values of t obtained from t/λ are higher than those obtained from the sums of the Ti and V partial thicknesses. In all cases, the maximum difference is ~1.5 nm irrespective of the precipitate thickness and decreases with the precipitate thickness, dropping to zero outside the precipitate. There is no definitive explanation for these differences in thicknesses. One possible explanation is that they are related to the stray signal present in the low loss [11, 16]. Another possibility is a slight error in the removal of the surface oxide contribution. Either could result in a small excess contribution in the low loss region after the subtraction of the matrix and a-C contributions, either of which will cause an apparent increase in thickness.

5.5. Determining the edge of the particle and particle volumes

Looking at the maps in Figure 4 or the line profiles in Figures 7 and 9, it is not easy to determine the position of the edge of the precipitate and hence its dimensions. In order to quantitatively determine the edge position, a mask is made from the (Ti+V) thickness map so that its value is 1 for thickness above a threshold and zero below it. The threshold is then adjusted until all the pixels in the "matrix" are at zero in the mask. Unfortunately, such a mask often looks bigger than the size of the precipitate apparent from the map. The threshold can certainly be raised until the size of the map matches the perceived size but what is needed is a better way of making this judgement.

One way to do this is to start with the mask which matches the perceived size of a precipitate. From this mask a series of annular masks can be created, each nominally one pixel wide. A simple way to do is to apply a 3x3 smoothing filter to the starting mask and generate two more masks by using thresholds of 0.05 and 0.95, which gives masks one pixel larger and smaller respectively. The process can be repeated to cover the whole field of view. Subtracting the appropriate masks then gives the annular masks. Occasionally, a few pixels are common to two masks or a pixel is not included in any mask but these effects can be corrected. The first row of Figure 10 shows the sets of such annular masks for the four

precipitates. The values in every second mask have been set to zero so that the full set of masks can be seen.

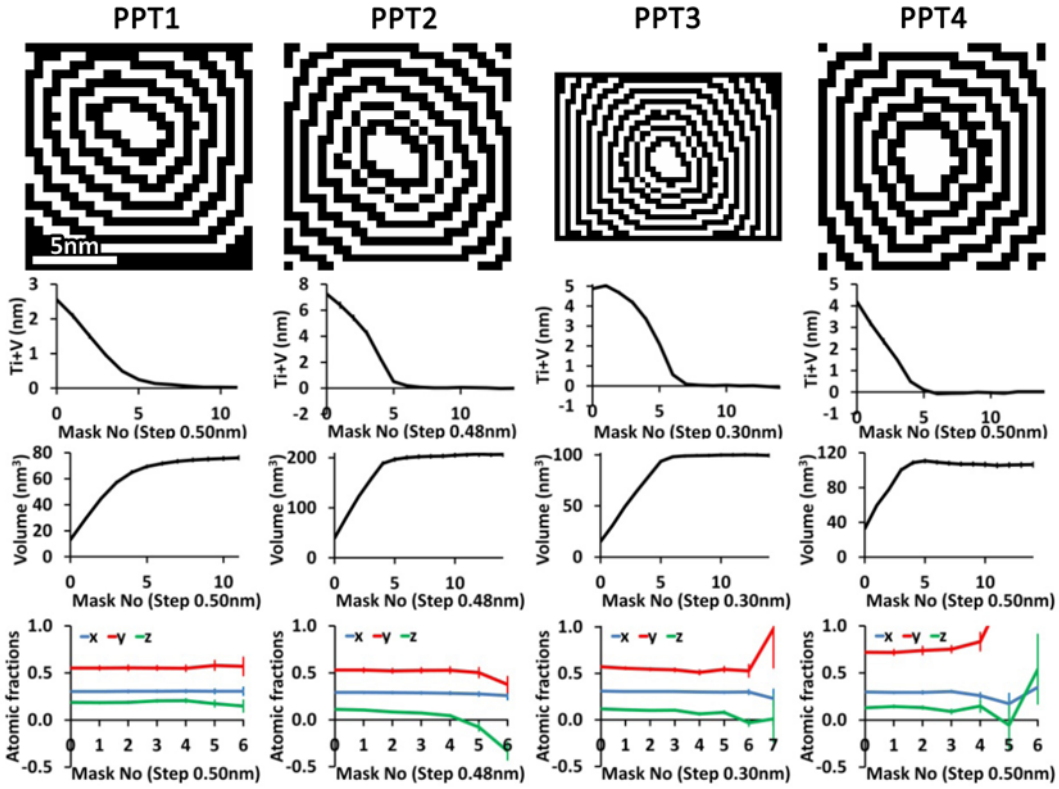

Figure 10. The first row shows the set annular masks used to analyse the behaviour with distance from the precipitate centre. All have the same horizontal scale. The second row shows the average (Ti+V) thickness in each mask. The spatial step associated with moving from one mask to the next is shown. The error bars, corresponding to the standard errors, are mainly smaller than the line thickness. The third row shows the cumulative volume of the precipitate as the contributions of successive masks are added. Again the standard error bars are small. The fourth row shows the atomic fractions x, y and z in $Ti_xV_{(1-x)}C_yN_z$. The error bars show the standard errors.

After the (Ti+V) thickness map is multiplied by one of the masks, the mean thickness, its standard deviation and its standard error can be calculated for the pixels in this mask. The mean thickness and its standard error are plotted as functions of mask number in the second row of Figures 10. Mask 0 corresponds to the central region of the precipitate. The spatial step corresponding to a change of mask number is the pixel size. The pixel sizes in Precipitates 1, 2, 3 and 4 are 0.50, 0.48, 0.30 and 0.50 nm, respectively.

For Precipitates 2, 3 and 4, the behaviour is relatively "ideal" in that the average thickness drops to "zero" above a given mask number. The last mask with a non-zero value determines the "edge" of the precipitate and this is mask 5, 6 and 4 for Precipitates 2, 3 and 4 respectively. For Precipitate 1, the mean thicknesses outside the precipitate are not "zero" and the values decrease approximately linearly with mask number. Projecting this slope back towards lower mask numbers shows that mask 5 is above this trend and so is taken as the "edge" of the precipitate.

The volume of the precipitate within a mask can be found by summing the thicknesses and multiplying the result by the area of the pixel. Starting from the values in the central mask, the third row of Figure 10 shows plots of the cumulative volumes of the precipitates as the contributions in subsequent masks are added. The corresponding standard error bars are shown. Precipitate 3 shows the most "ideal" behaviour with the volume curve having a plateau above its "edge". For Precipitates 2 and 4, there is a little positive and negative slope respectively but the change of volume after the "edge" is small. For Precipitate 1, there is no sharp change of slope at the "edge" but there is a clear roll-off in gradient from this point. In addition, the change in volume between the value including the "edge" mask and that including the next mask is small.

The masks can also be applied to the V, Ti, C and N thickness maps. This allows x, y and z in $Ti_xV_{(1-x)}C_yN_z$ to be found in each of the mask regions. These values are plotted as a function of mask number in the fourth row of Figure 10 along with the corresponding standard error bars. In each case, the plot is taken out to one mask beyond the "edge" of the precipitate. For the mask beyond the "edge", it is clear that the values become severely affected by the noise in the individual mean thicknesses.

The composition varies a little from precipitate to precipitate and this is likely to reflect minor inhomogeneities in the steel. The values of $(y+z)$ are less than unity as expected in these precipitate and the values are consistent with those found in VC_x, the dominant binary component.

Overall, the plots show that the precipitates are essentially homogeneous in composition. There is a hint that the Ti fractions and possibly the N fractions may decrease towards the edges of the precipitates. Such an effect would be plausible as both Ti and N are only present at low concentration in the matrix and so may be used up by the point that the

precipitates have grown to this size. However, the discussion in §6 shows that a systematic error may the cause of such slopes.

Table 1 summarises the findings of the analysis. Line 1 gives the values of the mean t/λ of the matrix for the four precipitates. From these and the value of $(t/\lambda)_S$ of 0.1 found in §4.2, the values of $(t/\lambda)_B$ for the matrix bulk can be found. The λ values for the bulk and surface are given by the Iakoubovskii parameterisation [31] applied to Fe-20%Mn and Fe_3O_4 respectively The 20% downwards correction found experimentally for $TiC_{0.98}$ has been applied [16]. As this correction has not been shown to apply to other compounds, there is still an uncertainty of this order in these two λ values. Lines 2 and 3 of Table 1 give the surface and bulk thicknesses of the matrix.

Line 4 gives the mean values of the thicknesses of the precipitates and their standard errors. These are not taken from the plots in Figure 10 since the Mask 0 positions do not necessarily coincide with the regions of maximum thickness. Instead, appropriate regions on the (Ti+V) thickness maps are selected and the means and standard deviations calculated.

Finding the lengths (maximum linear dimension) and widths (minimum linear dimension) of the precipitates is not straightforward. For a given mask, there is a certain amount of subjectivity in choosing the values. In addition, the mask defining the "edge" probably over-estimates the linear dimension as only a fraction of its pixels may contain signal from the precipitate. The next smaller mask certainly underestimates the linear size. Lines 5 and 6 give the lengths and the widths of the precipitates. The lower bounds are taken from the masks one smaller than the "edge" masks while the upper bounds are taken from the "edge" mask. There is typically a difference of ~10% between the lower and upper bounds but occasionally it is lower or higher

The projected area of the precipitate can be found by summing the pixels in all the masks covering the precipitate and multiplying the sum by the area of the pixel. Line 7 gives lower and upper bounds. The upper bound includes pixels in the "edge" mask and the lower bound excludes them. The difference between the upper and lower bounds is 30-40%.

Line 8 gives the volumes in all the masks out to the "edge" masks together with their standard errors. It is clear from Figure 10 that the "edge" mask contains pixels contributing to the volume and so should be included in calculating the volume. The values in brackets show the effect on the volume of adding the contributions of the pixels in the next larger

mask. For Precipitates 2, 3 and 4, the increase is the same or less than the standard error. For Precipitate 1, the increase is bigger, in line with the issues noted above. Lines 9, 10 and 11 give the mean values of x, y and z in Mask 0 and their standard errors.

	Precipitate	1	2	3	4
1	Mean t/λ	0.149	0.259	0.315	0.425
2	t matrix surface (nm)	10.1	10.1	10.1	10.1
3	t matrix bulk (nm)	4.5	14.5	19.7	29.7
4	t PPT (Mean Max) (nm)	2.76 ± 0.03	8.21 ± 0.07	5.14 ± 0.07	4.66 ± 0.07
5	Length (nm)	8.9 – 9.9	8.3 – 10.2	5.8 – 6.4	7.9 – 7.9
6	Width (nm)	7.9 – 8.9	6.9 – 8.7	5.5 – 6.4	6.9 – 7.9
7	Area (nm^2)	52 – 70	41 – 57	25 – 33	38 – 55
8	Volume (nm^3) (Volume including next mask)	69 ± 1 (72)	104 ± 2 (105)	98.2 ± 0.8 (98.9)	109 ± 2 (111)
9	x (mean at centre)	0.304 ± 0.005	0.293 ± 0.006	0.310 ± 0.004	0.298 ± 0.005
10	y (mean at centre)	0.55 ± 0.01	0.53 ± 0.01	0.57 ± 0.01	0.72 ± 0.02
11	z (mean at centre)	0.189 ± 0.006	0.111 ± 0.004	0.118 ± 0.008	0.13 ± 0.01

Table 1 Summary of the results found for the four precipitates.

6. Discussion

The values of the lengths, widths and thicknesses of Precipitates 2, 3 and 4 given in Table 1 show that these precipitates are reasonably equiaxed. However, the thickness of Precipitate 1 is less than its lateral dimensions. For Precipitate 1, the lamella is the thinnest. As the density of Fe_3O_4 is approximately half that of the matrix, the thickness of the un-oxidised lamella is the thickness of the bulk lamella plus half the thickness of the oxide in Table 1. Thus the thickness of this lamella at the end of the FIB milling process is 9.6 nm. The average of the four estimates of the linear dimensions of the precipitate size in Table 1 is 8.9 nm. Thus, unless the centre of the original precipitate was very close to the centre of the original lamella, the precipitate surface was exposed and it will have been thinned during the

milling. This may be related to the a-C associated with the precipitate in Figure 3. If this is the case, it suggests that Precipitate 4 is also close to the surface of the lamella as it too shows associated a-C in Figure 3. Precipitate 4 also shows a thickness smaller than its lateral dimensions supporting this interpretation.

The edges of the precipitates are hard to define. Also, the projected shapes vary from precipitate to precipitate because the actual shapes and/or the directions of projection differ. Thus it is hard to get accurate measurements of the lateral linear dimensions and the projected areas. There are more sophisticated ways of assigning values to these measurements but some underlying uncertainties will remain. On the other hand, the measurements of the thickness and the volume are far more precise. The average measured maximum thicknesses in the centres of the precipitates have standard errors which are a fraction of the lattice parameter. The volumes have a standard error of <2% and are sensitive to the choice of the edge by a similar amount. The reason for the insensitivity of the volume to the position of the edge is that the pixels at the edge have low values of thickness and so contribute little to the total volume.

In rows 2 and 3 of Figure 10, Precipitate 1 shows significant positive "tailing" of the precipitate signals into the matrix. The equivalent figures for Precipitate 3 show no such tailing while those for Precipitates 2 and 4 show low levels of positive and negative tailing respectively. This tailing is still present if the number of components used in the PCA noise reduction is increased and so it is not a PCA artefact. Dividing the annular masks into four quarters and redoing the analysis shows that the tailing is present in the top two quarters but absent in the bottom two quarters. One interpretation is that the tailing is a FIB artefact resulting from "re-deposition" when this precipitate was exposed and underwent thinning. An alternate interpretation is that the precipitate was still forming when the sample was quenched and that we are seeing a real diffusion profile of Ti and V in the area to one side of the precipitate.

While the thickness and volume measurements give a good representation of the precipitates in the lamella, it must be borne in mind that they can be subject to uncertainty because of the possibility of the precipitate having been thinned. Only the statistics from the analysis of a large number of precipitates or tilt experiments on individual precipitates could remove this uncertainty.

It is also worth looking at the standard deviations of the partial thicknesses in the different masks. The first row in Figure 11 plots the values against mask number. (The step sizes of the masks are shown on the figure.) For masks outside the precipitate, the standard deviations for a given element are relatively constant. However, for masks within the precipitates, the standard deviations for (Ti+V), V Ti and C increase. The reason for this is that the masks are not aligned with the loci of constant precipitate thickness. Thus the pixels within a mask will contain real thickness variations as well random variations, increasing the standard deviations measured. This interpretation is supported by the drop in the standard deviation in Mask 0 for each precipitate. Mask 0 covers a region of more slowly varying thickness in the centre of the precipitate so that the thickness variation is reduced. In addition, for precipitate 3, the region of low standard deviations extends over several masks near the centre. The reason for this can be seen in the maps in Figure 2 and the profiles in Figures 7 and 9, which show that the thickness near the centre of Precipitate 3 is relatively constant. Hence the effect of thickness variation on the standard deviation is much reduced. One implication of this is that the standard errors plotted in rows two and four of Figure 10 are overestimated in the regions where the thickness is changing. Those in row three are overestimated over the whole range since they are cumulative.

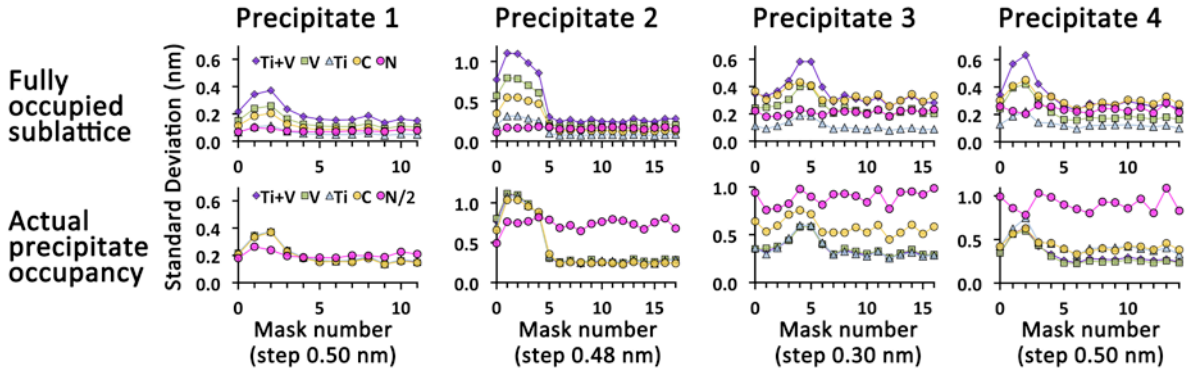

Figure 11. The standard deviations of the thicknesses in each annular mask. The spatial step associated with moving from one mask to the next is shown. The measurements in the first row correspond to cells with sub-lattice fully occupied by a single atom type. In the second row, the sub-lattice occupancies correspond to those in the actual precipitates. Note that the standard deviations for N in the second row are plotted as half their actual values to keep them on the same range as the other values.

In the first row of Figure 11 it is hard to discern a pattern in the standard deviations for the different elements. This is because they apply to partial thicknesses where the elements

are assumed to be present at all sites on their sub-lattice. However, the elements in the actual precipitates are only present on fractions of their sub-lattices sites i.e. (1-*x*), *x*, *y* and *z* for V, Ti, C and N respectively. Dividing the partial thicknesses and the corresponding standard deviations by the fractional occupancies gives the corresponding thicknesses of the actual precipitates and their normalised standard deviations. The second row of Figure 11 plots these normalised standard deviations against mask numbers making the trends much clearer. Note that the normalised standard deviations for N are plotted at 0.5 of their actual values in this row.

The first point to note is that the normalised standard deviations for N are higher than the others and tend not to show the peak due to the thickness change effect discussed above. This is expected as the N signal is the weakest and so the noise in it is more important than the thickness variations present in a given mask. Hence it has a higher, more constant standard deviation. The values for Precipitates 2, 3 and 4 are very similar. That for Precipitate 1 is a factor ~4 lower. The reason for this is not clear but part of the explanation lies in the fact that the Precipitate 1 is in a region where the matrix is thinnest and where the surface oxide is more than twice as thick as the bulk matrix.

The second point is that the normalised standard deviations for the V, Ti and C are now bunched together. For Precipitates 1 and 2, they fall on top of each other. For Precipitate 3, those for the metals fall on each other but those for C are a little higher while having a similar shape. For Precipitate 4, (Ti+V) and V overlie each other as do Ti and C but with larger values but again with a similar shape. The reasons for this are not clear.

For the four elements, the distributions of the thickness values in the background regions of the thickness maps are all good approximations to Gaussians. The standard deviations of these distributions allow estimates of the detection sensitivities to be made. Any pixel containing a value of thickness greater than four times the standard deviation has only a 1 in 15,000 chance of occurring in a Gaussian distribution. Since the background regions contain ~1000 pixels, this is a reasonable choice for the detection limit. For the four matrix regions, Figure 12a plots the number of unit cells of the $Ti_xV_{(1-x)}C_yN_z$ precipitate required for detection when using the signal from a given element. The thicknesses of the bulk and the surface oxide are shown separately. In the annular masks outside a precipitate, there is a distribution of standard deviations. The error bars on Figure 12a are the standard deviations of these distributions.

Detection using the N K-edge requires a large number of unit cells because of the low occupancy of the sub-lattice by N. For the other elements, typically two unit cells are required dropping to one in the thinnest matrix region. This drop is almost certainly related to the large oxide to bulk thickness ratio reducing the background in the spectrum.

The data is re-plotted in Figure 12b as if the sub-lattices were fully populated, corresponding to the measurements of partial thicknesses above. For Ti, the detection limit increases monotonically from 0.5 to 1.1 unit cells as the matrix thickness increases, whilst for V it increases from 1 to 2 unit cells. The most probable reason for larger values for V is the proximity of the O K-edge to the V $L_{2,3}$-edge. Separating these in the presence of noise will increase the uncertainty. The sensitivity for V is in line with that seen in earlier work where V(C,N) precipitates down to ~1 nm in size were detected [3].

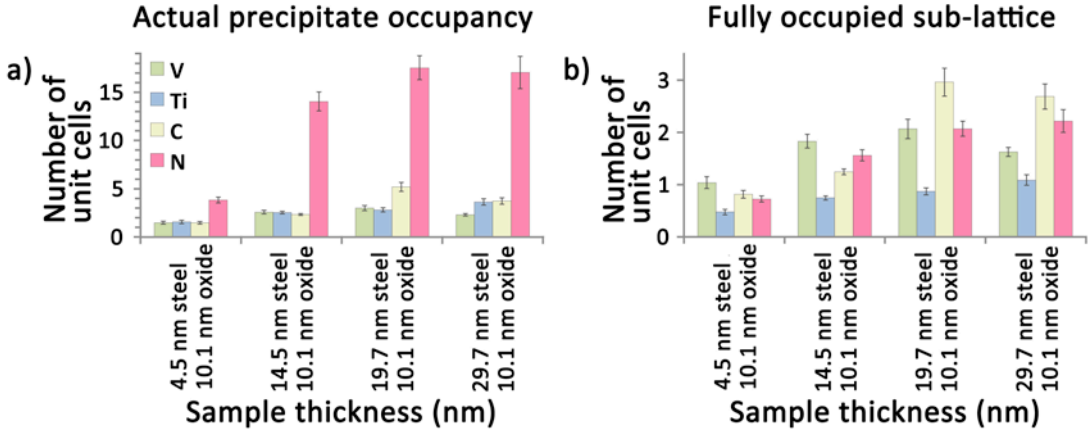

Figure 12. The number of unit cells required for detection by the signal from a given element at different matrix thicknesses. The matrix thickness is expressed as the sum of the bulk thickness plus the oxide thickness. a) For cells of the composition of the precipitate. b) For cells in which the sub-lattice is fully populated by the element. The error bars are the standard deviations of the distributions of standard deviations in the annular masks outside the "edge" mask.

The number of unit cells required when using the C or N K-edges tend follow each other with the number for N tending to be lower than that for C. The most probable reason for the higher value for C is that the C K-edge from the precipitate has to be separated from those from the C in the matrix and a-C on the surface, again increasing the uncertainty. The number of unit cells required for detection using the C K-edge starts below that required for detection by the V L-edge but eventually exceeds it as matrix thickness increases. The reason for this is likely to be that, as the thickness of the matrix increases, the number of O

atoms remains the same but the number of C atoms from the matrix increases. However, it is not clear why the N K-edge shows similar behaviour, albeit at a slower rate.

Turning to the errors on the results, the analysis using the annular masks gives errors on the result e.g. the random errors on x and y are in the range 1 – 2% irrespective of the mean matrix thickness while those for z start at 3% in the thinnest matrix and rise monotonically to 8% in the thickest. However, there will be systematic errors as well. Such systematic effects could arise at any point in the acquisition and processing of the data e.g. channelling, X-ray spike removal, PCA, and MLLS fitting.

In neither the acquisition of the steel data nor that for the experimental cross-sections was the crystallographic orientation of the specimen determined. However, a check on the effect of orientation on the cross-section was made for one of the standards [16]. This shows that the maximum variation in the cross-section for a range of orientation was typically <4% over the energy range of interest and reached a maximum of ~7% for one particular orientation. Thus it is reasonable to take 4% as an upper limit of the error from this source. Any other systematic errors in the cross-sections are believed to be less than this and should match equivalent systematic errors in the steel data. Thus they should cancel. One of the key benefit of using standards recorded under the same conditions as the steel data is that it achieves this cancellation.

When investigating the "tailing" of the precipitate signal into the matrix region around Precipitate 1 discussed above, the effects of changing the threshold setting used to remove the x-ray spikes from the data and of changing the number of components used in the PCA noise reduction were investigated.

Increasing the threshold for the detection of X-ray spikes from the 5σ used for the results in Figure 10 to 10σ allows the smaller spikes to remain. When this done, the mean thickness in most masks within the precipitate increases and hence causes a steady increase in the integrated volume as shown in Figure S3a in the Supplementary Material. Overall, there is an increase of ~3% in the precipitate volume. It has a bigger effect on y and z causing them to drop significantly towards the edge of the precipitate, as shown in Figure S3b. Thus it is important to keep the threshold for the detection of x-ray spikes as low as possible.

Increasing the components used for reconstruction in the PCA noise reduction from [0-6] to [0-15] when using the lower threshold for X-ray spikes causes additional similar but

smaller effects, as shown in Figures S4a and b in the Supplementary Material. The additional increase in the precipitate volume is only ~1.5% and the additional decreases in the values of y and z are much smaller.

Given the 5σ threshold for X-ray detection used here, it is likely to be the number of components used in the PCA that determine the contribution to the systematic errors and these are similar to the magnitude as the random errors. From the dependence of y and z on these parameters, it is possible that the slopes seen in the plots in Figure 10 may be the result of such systematic errors rather than small changes in composition.

Using experimental cross-sections to fit to experimental data without using background subtraction, where possible, has given results with low random errors. However, MLLS fitting always gives a result and systematic errors will occur if there is a missing component in the fit. Here, it is believed that a sufficient number of components has been included in the fits. However, there are some energy regions where the residuals are not randomly distributed about zero from effects such as modification of the EXELFS due to the matrix-precipitate interface and modification of the ELNES due to the alloying of Ti and V in the precipitate. These effects may introduce systematic errors that are difficult to quantify although they are likely to be small given the quality of the fits and the wide energy range over which the fits are made.

More generally, it may be instructive to compare this work with what is possible using other techniques for mapping the chemistry of precipitates in steels or related materials. Energy dispersive X-ray analysis in the scanning transmission electron microscope is a powerful way to analyse the chemistry with nanoscale or even atomic resolution. However, it has not been extensively used for the characterisation of such small precipitates as are studied in this work. Where it has been used for steel precipitate characterisation, the transition metal content has sometimes been examined quantitatively using EDX, but the carbon or nitrogen has not [32]. This is sensible as carbon or nitrogen X-rays are low in energy and strongly absorbed in materials, making a quantification result very sensitively dependent on sample thickness, inclination and thus unreliable. The fact that the X-ray signal for the heavier elements easily fulfils the projection requirement, however, means that it is well suited to tomographic reconstruction [33] (this is possible with EELS but requires more work due to multiple scattering [34]). Energy filtered TEM is very useful for qualitative mapping of chemistry over large areas, although getting sub-nm resolution is difficult [35, 36] and true

quantification is hard. Thus, it has been used for mapping steel precipitation [37] (including by the current workers), but less frequently for quantitative analysis.

3D atom probe tomography (3DAP) has been shown to be a powerful technique for the quantitative analysis of precipitates in steels [4, 38-40] although quantitative determination of carbon content can be problematic due to the rapidity of carbon arrival at the detector [41]. Conventional EELS has been used previously to study precipitation in steels, for example using a *k*-factor approach by Courtois *et al.* [37], although a standards-based approach was also used by Wilson and Craven [6], in both cases using point analysis. This was then extended to a larger number of VN precipitates by Wilson *et al.* [5]. Subsequently, EELS spectrum imaging was used by Craven *et al.* for the study of VN precipitates [4], and a more basic standards-based quantification was used to determine the nitrogen content. The present work significantly extends the accuracy and reliability of quantitative EELS mapping in a very similar way to the way in which recent advances in 3DAP are increasing the reliability of that technique [38]. To sum up, 3DAP and EELS mapping are the most quantitative techniques for the analysis of precipitate composition, and can be combined to address the ambiguities and shortcomings of each technique [4].

A few words should be said about the limitations imposed by radiation damage in EELS analysis. Courtois *et al*. showed that point analyses on a precipitate could cause nitrogen loss after about 45 s. In our work, using the higher current density available on a modern aberration-corrected microscope, we found that exposures of a few seconds with the probe in one place could accomplish the same or worse. But, using the fast scanning with dwell times of ~ 50 ms at step sizes of 3-5 Å never caused this problem and we believe that that there is no evidence of any significant radiation damage in this work.

One weakness of both 3DAP and quantitative EELS mapping is that the areas analysed are small (generally volumes of the order of $(10\ \text{nm})^3$ are examined). Whilst this is excellent for quantitative chemistry, this is less good for precipitate statistical information. Moreover, such detailed studies say little about the interaction between precipitation and other microstructural features such as dislocations and interfaces, and thus about how the precipitation happened as a consequence of the thermomechanical processing and its likely influence on properties. Thus, it would be ideal to combine such detailed nanoanalysis with other studies that examine the microstructure and that examine chemistry at larger sample volumes, even if at poorer spatial resolution and with less quantitative information about

chemical composition. Whilst EFTEM may be useful in this respect, this usually still works at relatively high losses (e.g. ~ 500 eV for V precipitates) which means long acquisition times for data any reasonable spatial resolution over large areas. The authors of the present publication are currently working on alternative approaches for larger area mapping using EELS and this will be the subject of a future publication.

7. Conclusions

Using experimental cross-sections to give quantitative information on the composition, thickness and volume of nanometre-sized $Ti_xV_{(1-x)}C_yN_z$ in a steel matrix gives excellent results with good precision and an accuracy of a similar magnitude. To achieve this, it is necessary to include in the MLLS fitting procedure a sufficient number of components to describe the spectra in the data from the steel including for vanadium and titanium carbides, for C and N to allow variable stoichiometry, for the matrix and any oxide surface, and for carbon contamination, as well as components to fit spectrometer readout artefacts. This also avoids issues with the effects of ELNES and EXELFS on the background shapes by using experimental background shapes for the main components of the fit.

From the fit coefficients, the thickness and the values of x, y and z are obtained pixel by pixel with high accuracy and precision allowing reliable determination of the stoichiometry of a precipitate just a few nm thick, even when embedded in a sample > 40 nm thick. Use of annular masks around the precipitate provides average values and errors for the thickness volume and composition of the precipitates. The edge of the precipitate can be determined from the change in the slope of a thickness versus mask number plot. This allows the volume of the precipitate established with a precision of a few per cent and is far more precise than trying to establish the linear dimensions or the area. The values of x, y and z are obtained with a standard error of ~2-3% in the centre, with the errors on z being at the higher end. Towards the edge, these errors rise by a factor of ~3. The compositions of the precipitates studied were quite homogenous internally, although there is some small variation from precipitate to precipitate. The detection level for each element using a signal from a fully occupied sub-lattice is typically in the range of 1 to 2 unit cells.

As for the Fe-Mn matrix, the uniform nature of the surface oxide in most areas allows the contributions of the matrix and its surface oxide to be separated using spectra from regions of different thickness. The bulk contribution shows no O K-edge signal but a C K-edge from the C in the matrix. A success of this approach is that the contribution of the C in the

precipitate can be separated from both the contribution of the C in the matrix and any a-C on the surface. The surface oxide contribution shows the ELNES expected on the O K-, Mn $L_{2,3}$- and Fe $L_{2,3}$-edges in an oxide. The Mn:Fe ratio is much lower than in the bulk and C content is very low. Because of the noise on this weak signal, it is not possible to determine whether the C is incorporated in the oxide or a total of about ~1 nm a-C on the surfaces.

The approach used here could be adapted for the study of other systems and is not confined to precipitation in metals. Provided the "matrix" has a strong signal that is not present in the "precipitate", the signal from the "precipitate" can be extracted. If "particle" has a well-defined chemistry and standards are available then the quantification procedure should here should be applicable. One example would be a supported catalyst system where the support plays the role "matrix" and the catalyst particles that of the "precipitates".

Acknowledgements

We are grateful to the European Commission for funding this work via the Research Fund for Coal and Steel (Precipitation in High Manganese Steels, RFSR-CT-2010-00018 and Control of precipitation sequences during hot rolling to improve product uniformity of titanium containing high strength steels, RFSR-CT-2015- 00013). The sample used in this work was provided by ThyssenKrupp Steel Europe AG and we are particularly thankful to Dr Georg Paul for his support. This work was only possible because of the generous provision of the MagTEM facility by SUPA and the University of Glasgow. We would like to thank Paul Thomas and Bernhard Schaffer of Gatan for their help with the scripting and their advice and help on the use of Digital Micrograph.

Supplementary Materials

A separate file is provided containing further details of the analysis provided in this paper, including further details relating to figures 2, 4 and 10.

References

[1] T. Siwecki, A. Sandberg, W. Roberts, R. Lagneborg, in: A.J. DeArdo, G.A. Ratz, P.J. Wray (Eds.) Thermomechanical Processing of Microalloyed Austenite, TMS-AIME, 1982, pp. 163-192.
[2] D.C. Houghton, G.C. Weatherly, J.D. Embury, in: A.J. DeArdo, G.A. Ratz, P.J. Wray (Eds.) Thermomechanical Processing of Microalloyed Austenite, TMS-AIME, 1982, pp. 267-292.
[3] M. MacKenzie, A.J. Craven, C.L. Collins, Nanoanalysis of very fine VN precipitates in steel, Scr. Mater. 54 (2006) 1-5.

[4] A.J. Craven, M. MacKenzie, A. Cerezo, T. Godfrey, P.H. Clifton, Spectrum imaging and three-dimensional atom probe studies of fine particles in a vanadium micro-alloyed steel, Mater. Sci. Tech. 24 (2008) 641-650.
[5] J.A. Wilson, A.J. Craven, Y. Li, T.N. Baker, Dispersion strengthening in vanadium microalloyed steels processed by simulated thin slab casting and direct charging - Part 2 - Chemical characterisation of dispersion strengthening precipitates, Mater. Sci. Tech. 23 (2007) 519-527.
[6] J.A. Wilson, A.J. Craven, Improving the analysis of small precipitates in HSLA steels using a plasma cleaner and ELNES, Ultramicroscopy 94 (2003) 197-207.
[7] Y. Ishiguro, K. Sato, Determination of non-stoichiometric composition of complex carbon-nitrides in steel by measuring plasmon energy, Mater. Trans. JIM 37 (1996) 643-649.
[8] A.J. Garratt Reed, Quantitative microanalysis with high spatial resolution, in: L. G.W., J. M.H., D. P. (Eds.), The Metals Society, London, 1981, pp. 165.
[9] S.P. Duckworth, A.J. Craven, T.N. Baker, Electron-energy loss spectroscopy of small particles in vanadium steels, Inst. Phys. Conf. Ser. (1983) 339-342.
[10] C.P. Scott, D. Chaleix, P. Barges, V. Rebischung, Quantitative analysis of complex carbo-nitride precipitates in steels, Scr. Mater. 47 (2002) 845-849.
[11] J. Bobynko, I. MacLaren, A.J. Craven, Spectrum imaging of complex nanostructures using DualEELS: I. digital extraction replicas, Ultramicroscopy 149 (2015) 9-20.
[12] C. Jeanguillaume, C. Colliex, Spectrum-image - the next step in EELS digital acquisition and processing, Ultramicroscopy 28 (1989) 252-257.
[13] J. Scott, P.J. Thomas, M. MacKenzie, S. McFadzean, J. Wilbrink, A.J. Craven, W.A.P. Nicholson, Near-simultaneous dual energy range EELS spectrum imaging, Ultramicroscopy 108 (2008) 1586-1594.
[14] A. Gubbens, M. Barfels, C. Trevor, R. Twesten, P. Mooney, P. Thomas, N. Menon, B. Kraus, C. Mao, B. McGinn, The GIF Quantum, a next generation post-column imaging energy filter, Ultramicroscopy 110 (2010) 962-970.
[15] R.F. Egerton, Electron Energy-Loss Spectroscopy in the Electron Microscope, Springer, New York, 2011.
[16] A.J. Craven, J. Bobynko, B. Sala, I. MacLaren, Accurate measurement of absolute experimental inelastic mean free paths and EELS differential cross-sections, Ultramicroscopy 170 (2016) 113-127.
[17] J. Verbeeck, S. Van Aert, G. Bertoni, Model-based quantification of EELS spectra: Including the fine structure, Ultramicroscopy 106 (2006) 976-980.
[18] J. Verbeeck, S. Van Aert, Model based quantification of EELS spectra, Ultramicroscopy 101 (2004) 207-224.
[19] M. Bosman, M. Watanabe, D.T.L. Alexander, V.J. Keast, Mapping chemical and bonding information using multivariate analysis of electron energy-loss spectrum images, Ultramicroscopy 106 (2006) 1024-1032.
[20] J. Spiegelberg, J. Rusz, K. Pelckmans, Tensor decompositions for the analysis of atomic resolution electron energy loss spectra, Ultramicroscopy 175 (2017) 36-45.
[21] F. de la Peña, T. Ostasevicius, V.T. Fauske, P. Burdet, P. Jokubauskas, M. Nord, E. Prestat, M.C. Sarahan, K.E. MacArthur, D.N. Johnstone, J. Taillon, J. Caron, T. Furnival, A. Eljarrat, S. Mazzucco, V. Migunov, T. Aarholt, M. Walls, F. Winkler, B. Martineau, G. Donval, E.R. Hoglund, I. Alxneit, I. Hjorth, L.F. Zagonel, A. Garmannslund, C. Gohlke, I. Iyengar, H.-W. Chang, HyperSpy v1.3, doi:10.5281/zenodo.583693 (2017).
[22] H.J. Goldschmidt, Interstitial Alloys, Butterworths, London, 1957.
[23] A.J. Craven, H. Sawada, S. McFadzean, I. MacLaren, Getting the most out of a post-column EELS spectrometer on a TEM/STEM by optimising the optical coupling, Ultramicroscopy 180 (2017) 66-80.
[24] G. Lucas, P. Burdet, M. Cantoni, C. Hebert, Multivariate statistical analysis as a tool for the segmentation of 3D spectral data, Micron 52-53 (2013) 49-56.
[25] J. Bobynko, Quantification of precipitation of carbides in V- and Nb- microalloyed high manganese steels, PhD Thesis, University of Glasgow (2017).

[26] P.A. van Aken, B. Liebscher, V.J. Styrsa, Quantitative determination of iron oxidation states in minerals using Fe L_2,L_3-edge electron energy-loss near-edge structure spectroscopy, Phys. Chem. Miner. 25 (1998) 323-327.
[27] L.A.J. Garvie, P.R. Buseck, Ratios of ferrous to ferric iron from nanometre-sized areas in minerals, Nature 396 (1998) 667-670.
[28] L.A.J. Garvie, A.J. Craven, High-resolution parallel electron-energy-loss spectroscopy of Mn $L_{2,3}$-edges in inorganic manganese compounds, Phys. Chem. Miner. 21 (1994) 191-206.
[29] J.D. Venables, D. Kahn, R.G. Lye, Structure of ordered compound V_6C_5, Philos. Mag. 18 (1968) 177-192.
[30] K. Cenzual, L.M. Gelato, M. Penzo, E. Parthe, Inorganic structure types with revised space groups. I, Acta Crystallogr. Sect. B-Struct. Commun. 47 (1991) 433-439.
[31] K. Iakoubovskii, K. Mitsuishi, Y. Nakayama, K. Furuya, Thickness measurements with electron energy loss spectroscopy, Microsc. Res. Tech. 71 (2008) 626-631.
[32] M. Peterlechner, H. Rosner, E. Nembach, EELS analysis of the nitrogen content of carbide particles in a commercial gamma '-strengthened nickel-base superalloy, Scr. Mater. 107 (2015) 42-45.
[33] T.J.A. Slater, R.S. Bradley, G. Bertali, R. Geurts, S.M. Northover, M.G. Burke, S.J. Haigh, T.L. Burnett, P.J. Withers, Multiscale correlative tomography: an investigation of creep cavitation in 316 stainless steel, Sci. Rep.-UK 7 (2017).
[34] A. Al Afeef, J. Bobynko, W.P. Cockshott, A.J. Craven, I. Zuazo, P. Barges, I. MacLaren, Linear chemically sensitive electron tomography using DualEELS and dictionary-based compressed sensing, Ultramicroscopy 170 (2016) 96-106.
[35] W. Grogger, B. Schaffer, K.M. Krishnan, F. Hofer, Energy-filtering TEM at high magnification: spatial resolution and detection limits, Ultramicroscopy 96 (2003) 481-489.
[36] S. Lozano-Perez, J.M. Titchmarsh, M.L. Jenkins, Quantitative EFTEM measurement of the composition of embedded particles, J. Mater. Sci. 41 (2006) 4394-4404.
[37] E. Courtois, T. Epicier, C. Scott, EELS study of niobium carbo-nitride nano-precipitates in ferrite, Micron 37 (2006) 492-502.
[38] M.I. Hartshorne, C. McCormick, M. Schmidt, P. Novotny, D. Isheim, D.N. Seidman, M.L. Taheri, Analysis of a New High-Toughness Ultra-high-Strength Martensitic Steel by Transmission Electron Microscopy and Atom Probe Tomography, Metallurgical and Materials Transactions a-Physical Metallurgy and Materials Science 47A (2016) 1517-1528.
[39] Y.J. Zhang, G. Miyamoto, K. Shinbo, T. Furuhara, Quantitative measurements of phase equilibria at migrating alpha/gamma interface and dispersion of VC interphase precipitates: Evaluation of driving force for interphase precipitation, Acta Mater. 128 (2017) 166-175.
[40] D. Jain, D. Isheim, D.N. Seidman, Carbon Redistribution and Carbide Precipitation in a High-Strength Low-Carbon HSLA-115 Steel Studied on a Nanoscale by Atom Probe Tomography, Metallurgical and Materials Transactions a-Physical Metallurgy and Materials Science 48A (2017) 3205-3219.
[41] M. Thuvander, J. Weidow, J. Angseryd, L.K.L. Falk, F. Liu, M. Sonestedt, K. Stiller, H.O. Andren, Quantitative atom probe analysis of carbides, Ultramicroscopy 111 (2011) 604-608.

Spectrum imaging of complex nanostructures using DualEELS:

II. Absolute quantification using standards

Supplementary Material

Alan J. Craven, Bianca Sala, Joanna Bobynko and Ian MacLaren

School of Physics and Astronomy, University of Glasgow, Glasgow G12 8QQ, UK

Figure S1 shows the spectra from the four precipitates summed over 6x6 pixels regions in their centres. Figure S1b is the same as Figure 2a in the main paper. Also shown are the MLLS fits over the range 150 to 750 eV and the residuals multiplied by 5. The arbitrary intensity units are the same in all cases but the scales have been adjusted to take account of the different specimen thicknesses. In all cases, the residuals are low over the majority of the 150 to 750 eV fitting range. As discussed in the main paper, the residuals have some shape in the 150 to 200 eV energy range and in the vicinity of the edges, with the latter being most prominent in the case of Precipitate 2.

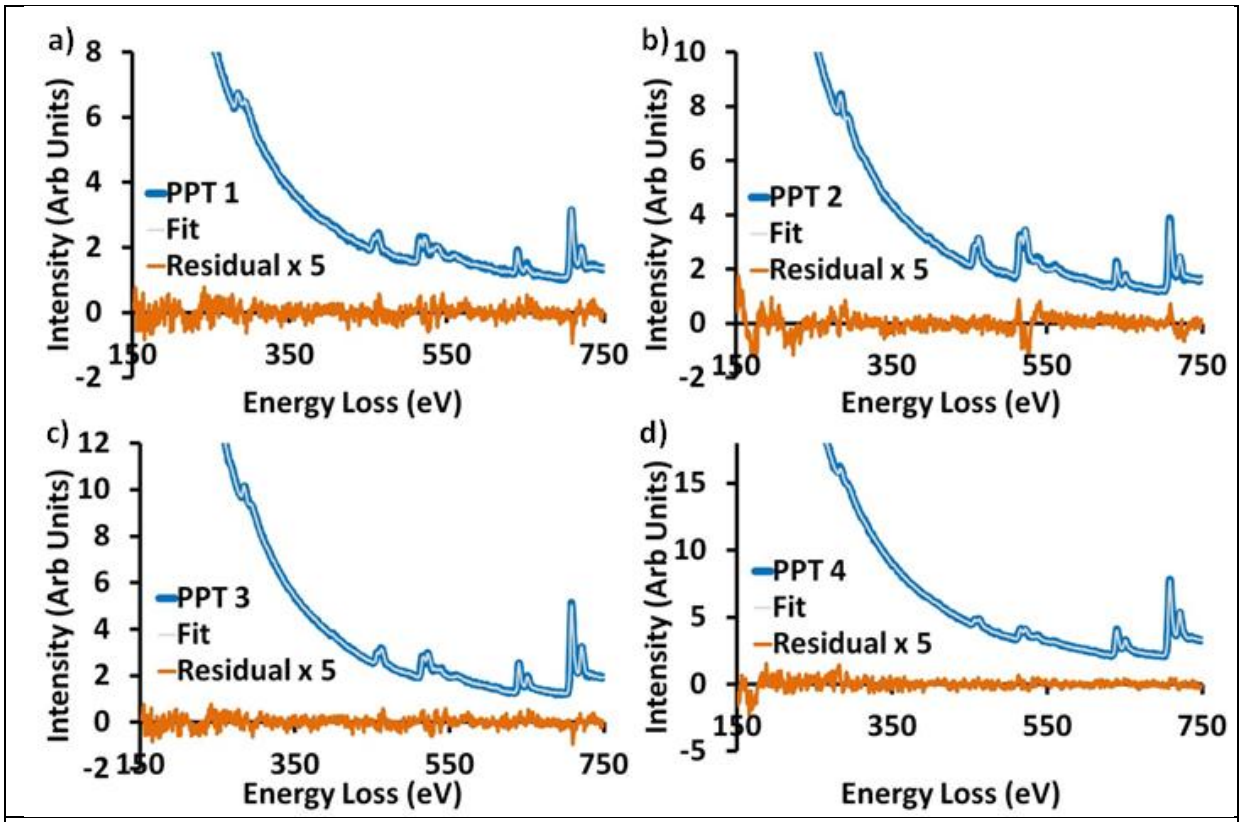

Figure S1. Fit and residual plots compared to the experimental plots for the central portion of each of the four precipitates presented in the paper.

Figure S2 shows the fit coefficient maps for the background, thin matrix, thick matrix, constant and step function components. In addition, the sum of the thin and thick matrix

components is shown. In the sum map, the positions of the precipitates are very clear whereas this is not the case in the individual thin and thick matrix component maps. This probably indicates a degree of fitting the noise in the data.

Figure S3 shows the effect of raising the threshold for the removal of X-ray spikes in the data from 5σ to 10σ so that some of the smaller ones are not removed. The solid lines are for the original threshold and the dashed lines are for the higher threshold. Figure S3a shows the effect on the integrated volume, which is small but does not take away the slow rise in the matrix region.

Figure S3b shows the effect on the *x*, *y* and *z*. The effect is negligible in Mask 0 where the signal is large but becomes very significant as the edge of the precipitate is reached. Thus keeping the threshold for the removal of X-ray spikes as low as possible is important.

With the higher 10σ threshold, Figure S4 shows the additional effect of increasing the components in the PCA reconstruction used for noise reduction from [0-6] to [0-15]. The solid lines are the same as the dashed lines in Figure S3 and the dashed lines show the additional changes. There is a similar but smaller additional change in the integrated volume but little further change in the values of *x*, *y* and *z*.

The implications of the results shown in Figures S3 and S4 are discussed in the main paper.

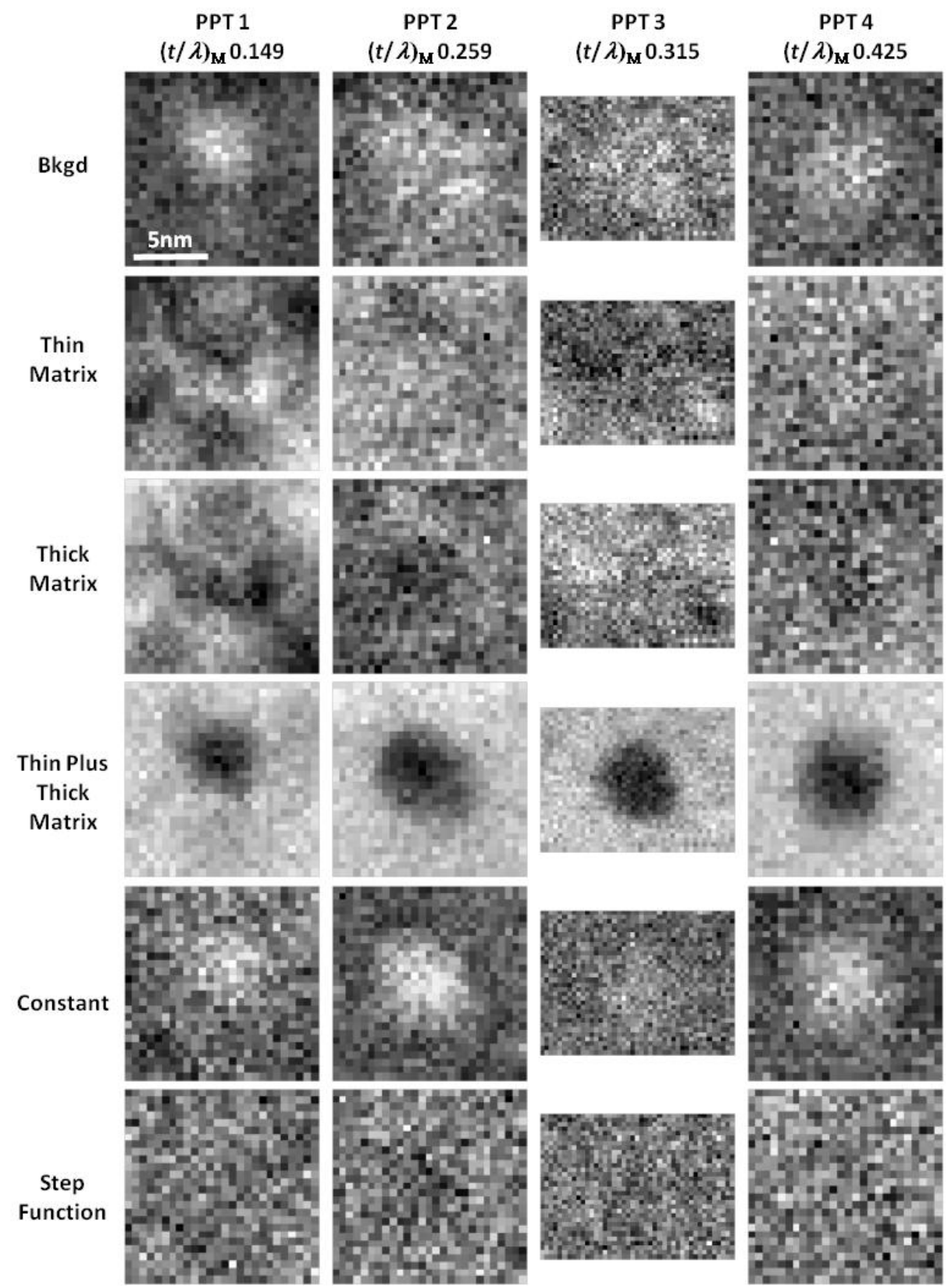

Figure S2 Maps of the fit coefficients for the background, thin matrix, thick matrix, sum of thin and thick matrix, constant and step function (horizontal direction) for the four precipitates (vertical direction). All the maps have the same spatial scale. The maps are to

show the spatial correlations and intensity scales are not given.

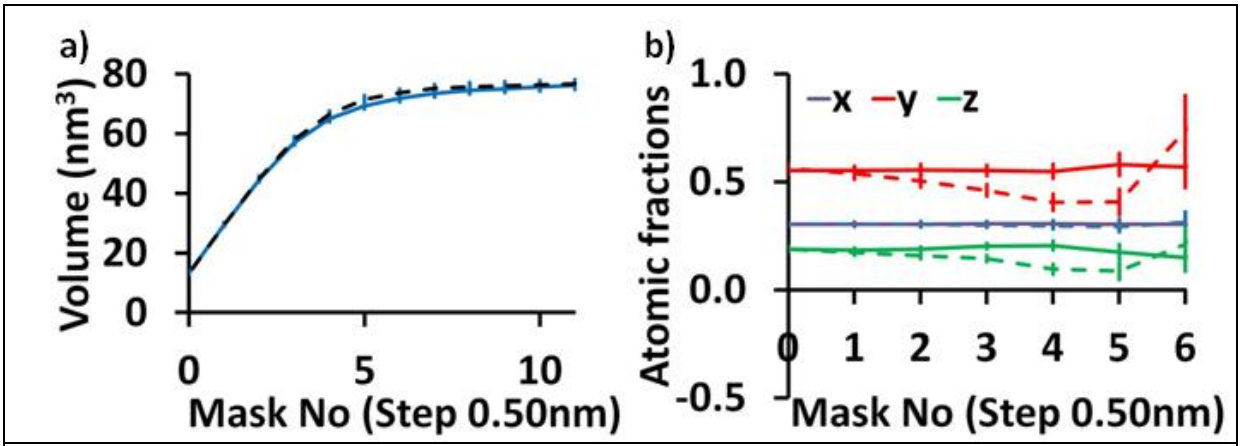

Figure S3. The effects of increasing the threshold for X-ray spike removal from 5σ to 10σ. The solid lines are the results for the 5σ threshold used in the main paper and the dashed lines are the results for the higher threshold. a) Integrated volume. b) Composition.

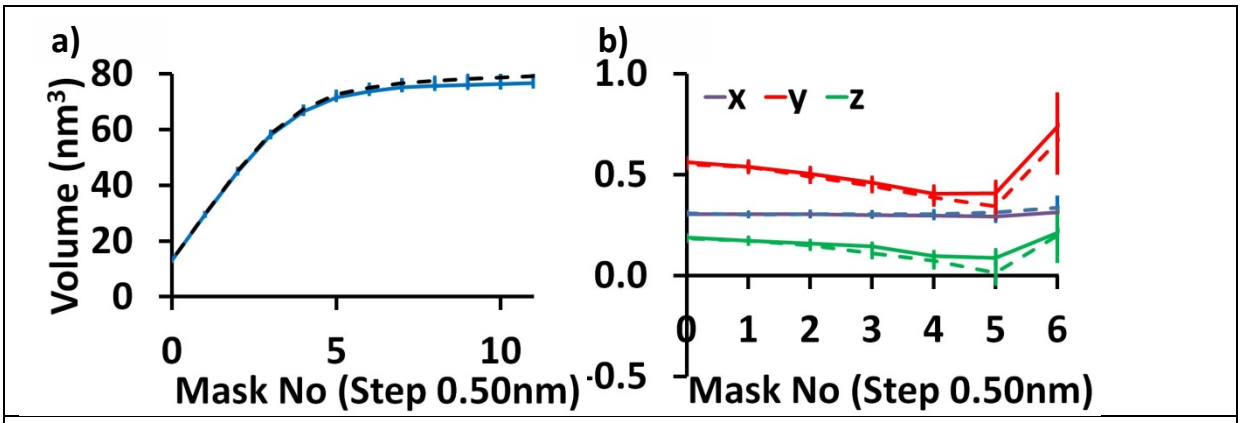

Figure S4. The effects of increasing the components used in the PCA reconstruction from [0-6] to [0-15]. The solid lines are the results for [0-6] with the higher 10σ threshold for X-ray spike removal i.e. the dashed lines in Figure S3. The dashed lines show the additional changes resulting from using [0-15] components in the PCA reconstruction. a) Integrated volume. b) Composition.